**Coupled Systems Mechanics,** *Vol. 11, No. 5 (2022) 411-438*
https://doi.org/10.12989/csm.2022.11.5.411 

# Viscoplasticity model stochastic parameter identification: Multi-scale approach and Bayesian inference

Cong-Uy Nguyen*[1,2], Truong-Vinh Hoang[3a], Emina Hadzalic[4b], Simona Dobrilla[1,2c], Hermann G. Matthies[2d] and Adnan Ibrahimbegovic[1,5e]

[1]*Royallieu Center of Research, University of Technology of Compiègne/Sorbonne University Alliance, France*
[2]*Institute of Scientific Computing, Technical University of Braunschweig, Germany*
[3]*Chair of Mathematics for Uncertainty Quantification, RWTH Aachen University, Germany*
[4]*Faculty of Civil Engineering, University of Sarajevo, Bosnia and Herzegovina*
[5]*Institut Universitaire de France, France*

*(Received April 1, 2022, Revised June 25, 2022, Accepted June 26, 2022)*

**Abstract.** In this paper, we present the parameter identification for inelastic and multi-scale problems. First, the theoretical background of several fundamental methods used in the upscaling process is reviewed. Several key definitions including random field, Bayesian theorem, Polynomial chaos expansion (PCE), and Gauss-Markov-Kalman filter are briefly summarized. An illustrative example is given to assimilate fracture energy in a simple inelastic problem with linear hardening and softening phases. Second, the parameter identification using the Gauss-Markov-Kalman filter is employed for a multi-scale problem to identify bulk and shear moduli and other material properties in a macro-scale with the data from a micro-scale as quantities of interest (QoI). The problem can also be viewed as upscaling homogenization.

**Keywords:** Bayesian update; Gauss-Markov-Kalman filter; inelastic and multi-scale problems; parameter identification

## 1. Introduction

The uncertainty quantification has been widely utilized in the field of computational mechanics. Many research works use this method to quantify the source of uncertainty in the numerical models. There are several sources of uncertainties in a numerical simulation, such as material and geometry uncertainties. In general, there are two common definitions, namely aleatory and epistemic uncertainties. The aleatory uncertainty is the inherent variation in a quantity

*Corresponding author, Ph.D., E-mail: cong-uy.nguyen@utc.fr
[a]Ph.D., E-mail: hoang@uq.rwth-aachen.de
[b]Professor, E-mail: emina_hadzalic@hotmail.com
[c]Ph.D. Student, E-mail: s.dobrilla@tu-bs.de
[d]Professor, E-mail: h.matthies@tu-bs.de
[e]Professor, E-mail: adnan.ibrahimbegovic@utc.fr


http://www.techno-press.org/?journal=csm&subpage=8 ISSN: 2234-2184 (Print), 2234-2192 (Online)

while the epistemic uncertainty is due to the lack of knowledge of an analyst. There are two popular problems in uncertainty quantification. The first one is the so-called forward problem, which is used to propagate the uncertainty through the model of interest and investigate the outputs, so that some of the key features or critical effects of inputs onto the model can be discovered. Meanwhile, the backward or inverse problem is employed to approximate the parameters of interest via the observed outputs of a given numerical model. In the later presented multi-scale problem, the data from the micro-scale can be used to assimilate data in the macro-scale, such process is known as upscaling. In contrast, the inverse one is named as downscaling.

Several researches relevant to the uncertainty quantification and analysis can be named as follows: dynamical systems in the frequency domain Römer *et al.* (2021), low-frequency electromagnetic devices Galetzka *et al.* (2019), sampling-free linear Bayesian update for fracture phase-field modeling Wu *et al.* (2021), Bayesian inference of heterogeneous visco-plastic material parameters Janouchova *et al.* (2018), stochastic multiple crack patterns Gerasimov *et al.* (2020), Polynomial chaos expansions for Maxwell's source problem Georg and Römer (2020), polynomial chaos in evaluating failure probability Janouchova *et al.* (2018), polynomial chaos for stochastic differential equations Xiu and Karniadakis (2002), adaptive Gaussian process for optimization problem Kim and Song (2021), inverse problem in piezoelectric material to identify damage Rus *et al.* (2006), structural fragility analysis underground motion Yi *et al.* (2019), and random fluctuations in material behavior of metals with visco-plastic and damage Kowalsky *et al.* (2007). There are several other researches adopting neural networks and machine learning into the engineering practices, e.g., solving phase-field modeling of fracture Goswami *et al.* (2020), predicting energy consumption Bui *et al.* (2020), detecting damage in wind turbine tower Nguyen *et al.* (2017), Nguyen *et al.* (2018), tracking high-dimensional non-Gaussian state models Hoang *et al.* (2021), modeling a digital twin for composite materials Ghanem *et al.* (2020), predicting load-bearing capacity of concrete-filled steel tubular Le and Le (2021), computational homogenization Nguyen *et al.* (2020), and calibration of nonlinear mechanical models Marevs *et al.* (2016), Kucerova and Leps (2014).

A cluster of research works is relevant to parameter identification, e.g., using conditional expectation Matthies *et al.* (2016), applying Gauss-Markov-Kalman filter for the Bayesian estimation Matthies *et al.* (2016), linear Bayesian updating Sarfaraz *et al.* (2018), developing sampling-free non-linear Bayesian update Matthies *et al.* (2016), considering stored energy and dissipation in multi-scale analysis Sarfaraz *et al.* (2020), applying the reduced model to quasi-brittle failure of concrete Ibrahimbegovic *et al.* (2020), estimating effective parameters in anisotropic hydraulic phase-field fracture Noii *et al.* (2020), estimating model coefficients of a novel turbulent flow model over porous media Friedman *et al.* (2016), developing an efficient computational method to sample the posterior random sets Hoang and Matthies (2021), stabilizing reduced order models in computational fluid dynamics problems Stabile and Rosic (2020), and Ivica Kožar *et al.* (2021). The idea of bring the parameter assimilation into the multi-scale problem is rather challenging. Some research works on multi-scale problems can be listed as probabilistic analysis of localized failure Ibrahimbegovic and Matthies (2017), efficient code-coupling strategy Ibrahimbegovic *et al.* (2014), embedded discontinuity capable of interpreting a full set of 3D failure modes for heterogeneous materials Ibrahimbegovic *et al.* (2014), programming and computational procedure Rukavina *et al.* (2019), poro-viscoelastic substitute model Jänicke *et al.* (2020), modelling of micromorphic continua Jänicke *et al.* (2009), elastic/viscoelastic compounds Schüler *et al.* (2013), micro-scale or nano-scale composites Chatzigeorgiou *et al.* (2015), curing processes Klinge *et al.* (2012), large eddy simulation of turbulent flow Gravemeier *et al.* (2010),

and Nitsche-type extended variational formulation for incompressible two-phase flow Schott *et al.* (2015). Nevertheless, there is a novelty in the current work, which presents a new approach to identify material properties by using simple and fast computation methods to apply on selective conventional mechanics problems.

The structure of this paper is outlined as follows. In Section 2, the theoretical background with a set of principle concepts and methods is laid out. To present an example, the fracture energy in a selective inelastic simulated via three-phases one-dimensional bar is chosen to be assimilated via the Bayesian update. In Section 3, the Gauss-Markov-Kalman filter is applied in a multi-scale problem with the visco-plasticity. The implementation is proceeded with an aim to upscale material properties in the macro-scale via data from the micro-scale. The micro-scale is simulated via the Lattice model, while the macro-scale is simulated via an enhanced triangular element using Raviart-Thomas vector space to interpolate the stress field with embedded capabilities of linear isotropic and kinematic hardening visco-plasticity. In Section 4, the conclusions are stated.

## 2. Theoretical background

In this section, the material properties at the micro-scale level are represented via the random fields. To numerically generate samples of such a random field, the Karhunen-Loève expansion can be employed. As an alternative to the density-based Bayesian update, the Gauss-Markov-Kalman filter is mainly used here for the upscaling problem. For that identification process, the above filter is conducted within the framework of Polynomial chaos expansion (PCE), where all random variables are formed via PCE. With this setting, the target material properties at macro-scale level are later updated via the Gauss-Markov-Kalman filter by using the observations of structural responses from the micro-scale level.

### *2.1 Micro-scale radom fields*

On the micro-scale, there is uncertainty about the exact composition and spatial arrangement. All model material properties are modeled via log-normal random fields so that they are guaranteed to be always positive. A random field (RF) is a collection of random variables and it explicitly depends on space and takes different value whenever it is observed. For example, two-dimensional sources of water or oil underground can be viewed as random fields. It can be stated that a random field is a mapping $\theta: (R^n, \omega) \to R$ with $n \geq 2$. Similar as the random variable, the mean value function is the most basic characteristic of a random field

$$\mu_\theta(\boldsymbol{x}) = E[\theta(\boldsymbol{x}, \omega)] = \int_\Omega \theta(\boldsymbol{x}, \omega) P(d\omega). \tag{1}$$

In a practical approach, the corresponding oscillating part $\theta(x, \omega) - \mu_\theta(x)$ is commonly represented via a linear combination of deterministic functions and coefficients, in which the latter can be random variables. There are several methods to separate the representation as above, such as the Karhunen-Loève expansion (KLE) and the Proper Orthogonal Decomposition (POD). In the following, only the Karhunen-Loève expansion (KLE) is discussed since it is one of the most common methods in the field of uncertainty quantification. The KLE can be employed for any random field, not just Gaussian one which is presented in this work. For the log-normal of such a

quantity, the spatial covariance is given by the Matérn-class, as it has independent variability in smoothness $v_c$ and correlation length $l_c$ as described correspondingly. Let us consider a random field in a two-dimensional domain Ω. It is clear that there is an infinite number of random variables at each point $x \in \Omega$ . The target is to reduce the number of these random variables by smoothening a given random field. In other words, it can be represented as a finite series of products of spatial functions multiplied by scalar random variables, in which the error with respect to the original random field can be neglected. Given a Gaussian stochastic field, the Karhunen-Loève expansion, see Smith (2013) and Chiachio-Ruano *et al*. (2021), is defined as

$$\Theta(x, \omega) = \mu_\Theta(x) + \sum_{i=1}^{\infty} \sigma_i \psi_i(x) \theta_i(\omega) \tag{2}$$

It can be seen clearly that Eq. (2) is composed of the first term as a mean value function $\mu\Theta(x)$ which depends only on space, and the second term as an oscillating part. The spatial functions $\psi_i(x)$ are square-integrable and orthogonal. $\theta_i(\omega)$ denotes independent standard Gaussian N(0,1) random variables, and the $\sigma_i$ are multipliers. The spatial functions $\psi_i(x)$ can be discretized in the spatial domain in a form as

$$\psi_i(\boldsymbol{x}) \approx \psi_{h\,i}(\boldsymbol{x}) = \sum_{j=1}^{n} \Psi_j(\boldsymbol{x}) v_{ji} = \boldsymbol{\Psi V} \tag{3}$$

in which $\boldsymbol{\Psi}$ is a matrix of spatial basis functions as shape functions in the finite element method. The optimal spatial functions are the solution of the generalized eigenvalue problem

$$\boldsymbol{GCG v}_i = \lambda_i \boldsymbol{G v}_i = \sigma_i^2 \boldsymbol{G v}_i, \tag{4}$$

in which $\lambda_i$ and $\boldsymbol{v}$ are the generalized eigenvalues and eigenfunctions. The $G(\Psi_i, \Psi_j)$ is the Gramian matrix of the basis functions, which can be assembled in the same manner as the mass matrix $\forall x \in \Omega$ as

$$\boldsymbol{G}(\Psi) = \int_\Omega \Psi_i(\boldsymbol{x}) \Psi_j(\boldsymbol{x}) d\Omega \tag{5}$$

Meanwhile, the covariance matrix $\boldsymbol{C}$ is computed via Matérn function between each couple of points, e.g., $C_{i,j} = C_{v_c}(d_{ij}/l_c)$. The Matérn function is defined as

$$C_{\nu_c}(d_{ij}/l_c) = \sigma^2 \frac{2^{1-\nu_c}}{\Gamma(\nu_c)} \left( \sqrt{2\nu_c} \frac{d}{\ell_c} \right)^{\nu_c} K_{\nu_c} \left( \sqrt{2\nu_c} \frac{d}{\ell_c} \right), \tag{6}$$

where $v_c$ is a non-negative parameter, $\sigma$ is also an input parameter, $d_{i,j}$ is the distance between the two input points $(i, j)$, and $l_c$ is the correlation length. The Gaussian $\Theta(x)$ field can be approximated

$$\Theta(\boldsymbol{x}, \omega) \approx \mu_\Theta + \sum_{i=1}^{L} \sigma_i \psi_i(\boldsymbol{x}) \boldsymbol{\theta}_i(\omega) = \mu_\Theta + \boldsymbol{\Psi}(\boldsymbol{x}) \boldsymbol{V S \theta}(\omega), \tag{7}$$

where $L \leq n$ is the truncated number of the eigenfunctions defined as

$$\rho_L = \frac{\sum_{i=1}^{L} \lambda_i}{\sum_{j=1}^{n} \lambda_j}, \tag{8}$$

in which *n* is the number of eigenvalues in a given system. The relative cumulative factor $\rho L$ can be predefined, normally $\rho L \geq 0.9$.

### *2.2 Bayesian update*

The non-intrusive and intrusive methods are common approaches for the uncertainty quantification analysis. The former is proceeded by treating the available finite element model, such as in-house codes or commercial computational programs, as black boxes. By contrast, the latter method heavily reformulates the weak form or variational formulation of the problem and introduces the uncertainty into the system explicitly. Hence, this approach is more complicated and sometimes it is impossible with a high number of uncertainty parameters due to the extreme complexity. Only non-intrusive methods are investigated to identify material properties in this paper. Specifically, the Bayesian updating method is adopted for the parameter identification. The inverse problem of identifying or calibrating the material properties in a given numerical model is addressed in the framework of the Bayesian estimation, which leads to a computation of the conditional expectation. The Bayesian theorem is considered as the consistent way to update a probabilistic description when new data in the form of observations $\mathcal{Y}$ are available. In such case, it is possible to state the conditional density $\pi(\theta|\mathcal{Y})$ of $\theta$ given $\mathcal{Y}$, see Tarantola *et al.* (2004), Matthies *et al.* (2016)

$$\pi(\theta \mid \boldsymbol{y}) = \frac{\pi(\theta, \boldsymbol{y})}{\pi(\boldsymbol{y})} = \frac{\pi(\boldsymbol{y} \mid \theta)}{\pi(\boldsymbol{y})}\pi(\theta), \tag{9}$$

in which

$$\pi(\boldsymbol{y}) = \int \pi(\theta, \boldsymbol{y}) d\theta = \int \pi(\boldsymbol{y} \mid \theta)\pi(\theta) d\theta, \tag{10}$$

where $\pi(\mathcal{Y})$ is the probability density function (pdf) of the random variable $\mathcal{Y}$ (the evidence) and $\pi(\theta)$ is the prior probability density function, and $\pi(\mathcal{Y}|\theta)$ is the likelihood of $\mathcal{Y} = Y(\theta, \in)$ given $\theta$, where $\epsilon$ is the observation error. The prior probability density function $\pi(\theta)$ describes a belief of an analyst about the possible population characteristics of the random variable $\theta$. The likelihood $\pi(\mathcal{Y}|\theta)$ describes our belief that the observations $\mathcal{Y}$ if we know $\theta$ is true. And the posterior $\pi(\theta|\mathcal{Y})$ describes our belief on the possible population characteristics of random variable $\theta$ after observing $\mathcal{Y}$.

The flow chart of the Bayesian updating method is shown in Fig. 1. Firstly, realization of each interest input variables is generated via its corresponding prior distribution. The prior probability density function can be selected from several available distributions so that it is mathematically feasible to generate the realization of a given random variable. Secondly, the target physics or mechanics problem can be cast in a general form of mathematical representation $M(\theta)$, which can be built via commercial computational programs or in-house codes. It can be also truncated and approximately represented via surrogate model, such as general Polynomial chaos (gPC) with a fast computational capability. In the following works, the model $M(\theta)$ is solved by finite element method, which is programmed as a FORTRAN user-defined element in the FEAP computational program. Then the quantity of interest (QoI) depends on the nature of the problem and the selection of an analyst. However, it is normally selected based on the criterion that it can be measured explicitly with the aid of experimental tools. The common examples of QoI are the displacement, velocity, acceleration, strain, reaction force, stored energy, and even dissipation.

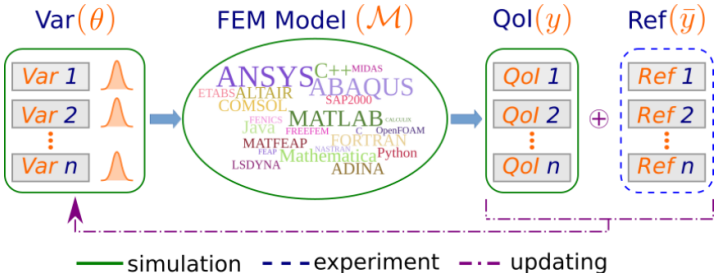


Fig. 1 Flow of Bayesian updating method

Table 1 One-dimensional inelastic bar material properties

| Property | A | E | $\sigma_y$ | $K_h$ | $\sigma_u$ | $K_s$ |
|---|---|---|---|---|---|---|
| Value | 1 | $30 \times 10^6$ | $30 \times 10^3$ | $15 \times 10^6$ | $60 \times 10^3$ | $7.5 \times 10^6$ |

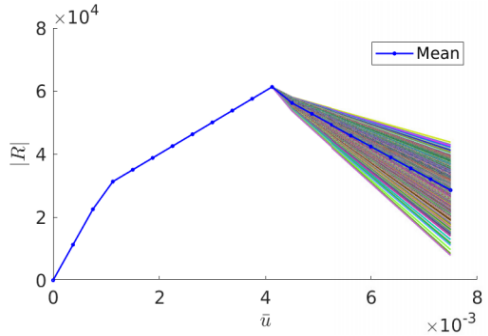


(a) Reaction vs displacement

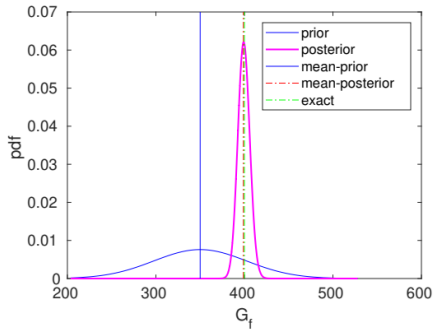


(b) Prior and posterior pdf of $G_f$

Fig. 2 Bayesian updating of $G_f$ using reaction $R_x$

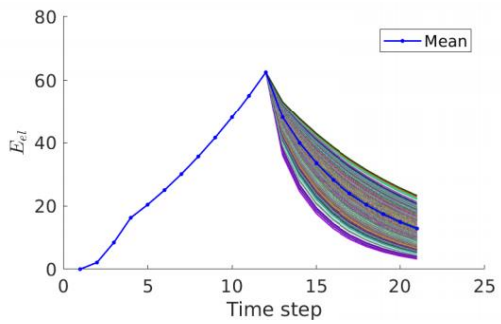


(a) Elastic energy $E_{el}$

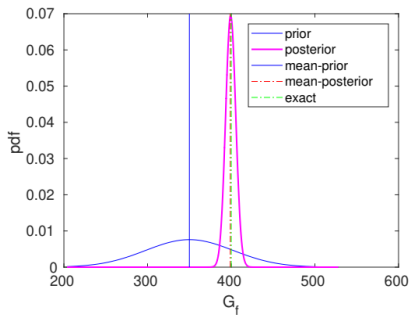


(b) Prior and posterior pdf of $G_f$

Fig. 3 Bayesian updating of $G_f$ using elastic energy $E_{el}$

Finally, with the data from the experiment, all essential ingredients are completed in the preparation for the Bayesian updating.

In the following, the Bayesian updating method is conducted to update the fracture energy $G_f$ under the softening regime in a one-dimensional coupled elasto-plasticity. A cantilever bar is fixed on the left and an imposed displacement $u$=0.01 is applied within 500 time steps on the right. The

Table 2 Prior, posterior and true values of fracture energy $G_f$

| Property | Prior $\mu_{Gf}$ | Prior $\sigma_{Gf}$ | Posterior $\mu_{Gf}$ | Posterior $\sigma_{Gf}$ |
|---|---|---|---|---|
| QoI: $R_x$ | $3.5 \times 10^2$ | 52.5 | 398.8 | 6.98 |
| QoI: $E_{el}$ | $3.5 \times 10^2$ | 52.5 | 398.9 | 6.29 |

reaction force and elastic energy at the last time step are selected as QoIs. The assumed true values of the material properties are given in Table 1, e.g., cross section area A, Young elastic modulus E, yield stress $\sigma_y$, linear hardening modulus $K_h$, ultimate stress $\sigma_u$, linear softening modulus $K_s$ and fracture energy $G_f$ in the case of exponential softening regime.

It is assumed that the prior distribution given to the plastic softening modulus $G_f$ is the Normal distribution $N(\mu_{Gf}, \sigma_{Gf})$ truncated such that $G_f$>100, in which the standard deviation $\sigma_{Gf} = 52.5$ is set to be 15% of a mean value $\mu_{Gf} = 35 \times 10^2$. The realization of $G_f$ is generated by Monte-Carlo method with $n_s = 10^3$ samples. With each value of the fracture energy $G_f$, the problem is executed once.

The responses from reaction and elastic energy are given in Fig. 2(a) and Fig. 3(a). As shown in Fig. 2(b) and Fig. 3(b), those updated standard deviations are much smaller than the prior counterpart. This means that after using the Bayesian updating method the updated value of the fracture energy is getting more accurate and reliable than the prior mean value of $\mu_{Gf}$. The collection of prior and posterior values of the fracture energy $G_f$ is summarized in Table 2.

The Bayesian update yields a conditional or posterior probability distribution from the prior one. This method requires high computation cost for large models. As an alternative, the Gauss-Markov-Kalman filter can perform better thanks to the approximation of the conditional mean or conditional expectation. The Kalman filter is introduced firstly as a base for the above filter. Let us consider again the mathematical or numerical model, such as finite element model, with $y = M(x)$ with $x \in X$. The task is now to calibrate or identify input parameter $x_a$ from a forecast $x_f$, representing initial knowledge, and an observation $\hat{y}$ for the random variable $z = Y + \epsilon$. The filtered or assimilated random variable $x_a$ after the observation $\hat{y}$ is given as

$$\boldsymbol{x}_a = \boldsymbol{x}_f + \left(E_X\left(\boldsymbol{x}_f \mid \hat{y}\right) - E_X\left(\boldsymbol{x}_f \mid z\right)\right) = \boldsymbol{x}_f + \boldsymbol{x}_i, \tag{15}$$

in which the term so-called innovation $x_i$ is actually an orthogonal error. It is observed that $x_a$ is unbiased and linear in $x_a$, while $E_X(x_f|\hat{y})$ is linear and optimal. The problem turns into finding the solution of the minimization equation, see Matthies *et al.* (2016), as

$$\left\|\boldsymbol{x}_f - \left(\boldsymbol{K}(z) + \boldsymbol{a}\right)\right\|_X^2 = \min_{\boldsymbol{L},\, \boldsymbol{b}} \left\|\boldsymbol{x}_f - \left(\boldsymbol{L}(z) + \boldsymbol{b}\right)\right\|_X^2, \tag{16}$$

in which $a = \bar{x}_f - \boldsymbol{K}(\bar{z})$. The Kalman gain $\boldsymbol{K}$ satisfies the above minimization problem, hence the final form of the Kalman filter is given as

$$\boldsymbol{x}_a = \boldsymbol{x}_f + \boldsymbol{K}\left(\hat{y} - z(\omega)\right) = \boldsymbol{x}_f + \boldsymbol{K}\left(\hat{y} - \left(M\left(\boldsymbol{x}_f(\omega)\right) + \epsilon(\omega)\right)\right), \tag{17}$$

in which the Kalman gain is computed as $\boldsymbol{K} = \boldsymbol{C}_{xfz}\, \boldsymbol{C}_z^{-1}$ and $\boldsymbol{C}_{xfz}$ is the covariance of $\boldsymbol{x}_f$ and $Z$, while $\boldsymbol{C}_z$ is the auto-covariance of $z$.

### *2.3 Polynomial chaos expansion*

A mechanics problem itself can be viewed as a mapping M, which can be a linear or nonlinear mapping depending on the nature of the given problem, from the input data *x* to the output data $\mathcal{Y}$ via relation $\mathcal{Y} = M(x)$. To obtain more insights into the given problem, the input data *x* can be formulated as random variables or also as random fields. After going through the mapping M, it is clear that the output data $\mathcal{Y}$ is no more deterministic but rather a stochastic or random one. The uncertainty in the input *x* can propagate thorough out the mapping M. More precisely the uncertainty propagation refers to mean value, variance, probability distribution and other quantities. Not only the forward propagation problem but also backward or parameter identification are of research interest. In practice, there are several methods to formulate the surrogate model of the mapping M. One of the most popular is so-called Polynomial chaos expansion (PCE), which is discussed briefly and employed for the process of updating in this section. More detailed discussion on PCE and generalized Polynomial Chaos can be referred to Xiu (2010), Xiu and Karniadakis (2002), and Ulrich (2021). The Polynomial chaos expansion (PCE) for a random variable $\mathcal{Y}$, which has finite mean value and variance ($E[\mathcal{Y}], V[\mathcal{Y}]) < \infty$, and corresponding probability density function $f_{\mathcal{Y}}$ is defined as follows

$$y = \sum_{i-0}^{\infty} q_i \Phi_i(\xi) \tag{11}$$

in which the involving polynomial must be orthogonal with respect to the probability density function $f_x$

$$E_\xi [\Phi_i \Phi_j] = \int_R \Phi_i(\alpha)\Phi_j(\alpha) f_\xi(\alpha) d\alpha = \delta_{ij}, \tag{12}$$

and the polynomials are normalized via

$$\int_R \Phi_i^2(\alpha) f_\xi(\alpha) d\alpha = 1. \tag{13}$$

If a random variable $\mathcal{Y}$ is represented via a Gaussian distribution basis function or germ $\xi(\omega) \sim N(0,1)$ then the corresponding polynomials are the Hermite functions because they are orthogonal with respect to the Gaussian distribution. Several computations can be executed via numerical integration instead of direct sampling. The coefficients of the PCE of the model can be obtained using output from the numerical model $\mathcal{Y}(\xi_j) = M(\xi_j)$ as follows

$$q_i \approx \frac{\sum_{j=1}^{n_{int}} \mathcal{Y}(\xi_j)\Phi_i(\xi_j)\,\omega_j}{E[\Phi_i(\,)^2]} \tag{14}$$

in which $(\xi_j, \omega_j)$ are numerical integration point *j* and its weight. The extension to the PCE of multi-variable $\mathcal{Y} = M(x_1, x_2, \ , x_n)$ is in the same manner with more germs and integration points. The essential mapping from germs $\xi$ to input parameter is omitted sometimes if it is an identity map, nevertheless the map is an injective function in general.

With the above discussion on the Polynomial chaos expansion (PCE) and the Kalman filter, the Gauss-Markov-Kalman filter is presented correspondingly, Juan *et al.* (2021), Rosic *et al.* (2012), and Rosic *et al.* (2014) for more detailed discussion and Marsili *et al.* (2015), Kumar *et al.* (2018) for the relevant approach. In the following framework of Gauss-Markov-Kalman filter, all relevant random variables in the model are represented via PCE. Hence the filter can be computed with

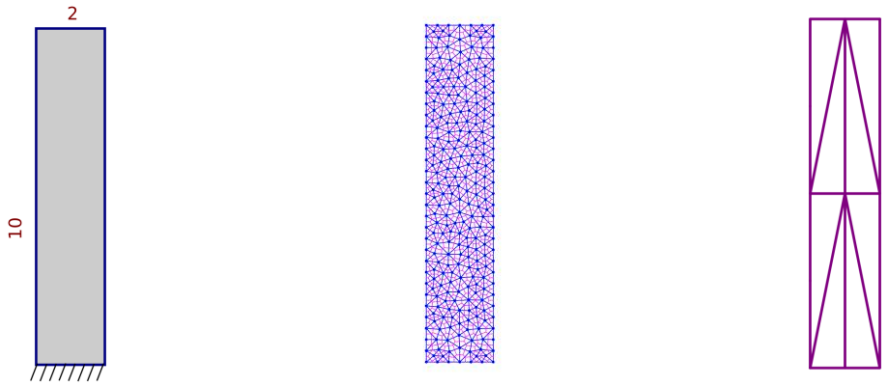


(a) (b) (c)

Fig. 4 Multi-scale setting: (a) Geometry, (b) Micro-scale: Lattice model, (c) Macro-scale: Enhanced triangular model

these PCE coefficients in order to update the PCE coefficients of the targeted random variables. This method is proceeded without any sampling work while there are other approaches, e.g the Ensemble Kalman Filter (EnKF), see Rosic (2014). The input parameter, the error and the measurement are written in the PCE format

$$q = \sum_{i=0}^{l} c_i^q \Phi_i^q(\xi), \quad \epsilon = \sum_{i=0}^{n} c_i^e \Phi_i^e(\eta), \quad y = \sum_{i=0}^{m} c_i^y \Phi_i^v(\xi) \tag{18}$$

The input parameter $q$ is introduced to generalize the problem with an additional map from $q$ and $x$ via $x = f(q)$, which can be essential for the latter updating non-negative material parameters. The input parameter $q$ and measurement $\mathcal{Y}$ are estimated via the same basis functions $\xi$, while the error is estimated via the different one $\eta$. Hence, it is required to fuse them all together so all considered variables are approximated by the same set of basis functions $(\xi, \eta)$. This transformation is given as follows

$$q = \sum_{i=0}^{h} \hat{c}_i^q \hat{\Phi}_i(\xi, \eta) = \hat{Q}\hat{\Phi}, \quad \epsilon = \sum_{i=0}^{h} \hat{c}_i^e \hat{\Phi}_i(\xi, \eta) = \hat{E}\hat{\Phi}, \quad y = \sum_{i=0}^{h} \hat{c}_i^y \hat{\Phi}_i(\xi, \eta) = \hat{\Upsilon}\hat{\Phi} \tag{19}$$

With the current PCE form of all random variables, the Kalman filter can applied directly as

$$\hat{Q}'\hat{\Phi} = \hat{Q}\hat{\Phi} + K(\hat{Z}\hat{\Phi} - (\hat{\Upsilon}\hat{\Phi} + \hat{E}\hat{\Phi})), \tag{20}$$

By removing the common basis functions $\hat{\Phi}$, the new filtered or assimilated PCE coefficients of input variables are written as

$$\hat{Q}' = \hat{Q} + K(\hat{Z} - (\hat{\Upsilon} + \hat{E})), \tag{21}$$

in which the Kalman gain is computed via following equation

$$K = C_{QY}\left(C_Y + C_E\right)^{-1}, \tag{22}$$

and corresponding covariance matrices are obtained directly from the PCE coefficients. The numerical implementation is proceeded via SGLIB library, see Zander (2011).

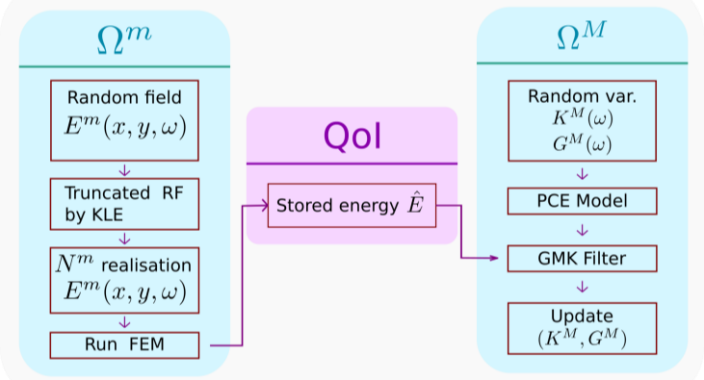


Fig. 5 Flow of data and update for upscaling in elastic regime

## 3. Parameter identification in multi-scale problem

In this section, the parameter identification is configured for a multi-scale problem, e.g., a micro-scale is simulated via the Lattice model while a macro-scale is simulated via a mixed triangular element with Raviart-Thomas interpolation. The geometry selected for the multi-scale problem is 2×10 in length and height as shown in Fig. 4(a). The corresponding mesh in the micro-scale and the macro-scale are shown in Figs. 4(b), (c).

There are 738 elements in the micro-scale and only 8 elements in the macro scale. As shown in Fig. 5, the micro and macro scales are denoted correspondingly as domain $\Omega^m$ and $\Omega^M$. One-way connection from $\Omega^m$ and $\Omega^M$ is the Quantity of Interest (QoI), which is computed from the micro-scale. In general, both bulk and shear moduli $K^m(x,y,\omega), G^m(x,y,\omega)$ can be considered as random fields in the micro-scale $\Omega^m$. In the case of vanishing Poisson ration, the shear modulus is a function of Young modulus, hence only Young modulus $E^m(x,y,\omega)$ is considered as a random field. This random field is then truncated via the Karhunen-Loève method to remove the high-order modes with its correspondingly low eigenvalues. Then one can use any sampling method to generate a set of $\mathrm{N}^m$ realizations for $E^m(x,y,\omega)$. The number of simulations is exactly the number of realizations $\mathrm{N}^m$. All of the QoI data, which can be stored energy $\hat{E}$ and dissipation $\hat{D}$, at each time step are saved for further updating procedure in the macro-scale $\Omega^M$.

Once the data QoI computed in the micro-scale is successfully processed, the updating procedure by the Gauss-Markov-Kalman filter in the macro-scale $\Omega^M$ can be started. This process can be viewed as a homogenization work, in which both bulk and shear moduli $(K^m(\omega), G^m(\omega))$ are parameters to be identified in the macro-scale $\Omega^M$. It is noted that those parameters are implemented as random variables, which are constant over the entire domain $\Omega^M$. The surrogate model using the PCE is applied for QoI in the macro-scale $\Omega^M$, which is necessary for the updating process by the Gauss-Markov-Kalman filter. The QoI from both scales is delivered into the procedure of the Gauss-Markov-Kalman filter with an aim to update the bulk and shear moduli of the current macro-scale $(K^M, G^M)$. All key tasks for this multi-scale problem are drawn in Fig. 5. In order to update other parameters in the macro-scale, the same procedure can be applied.

### *3.1 Setting the random fields at the micro-scale $\Omega^m$*

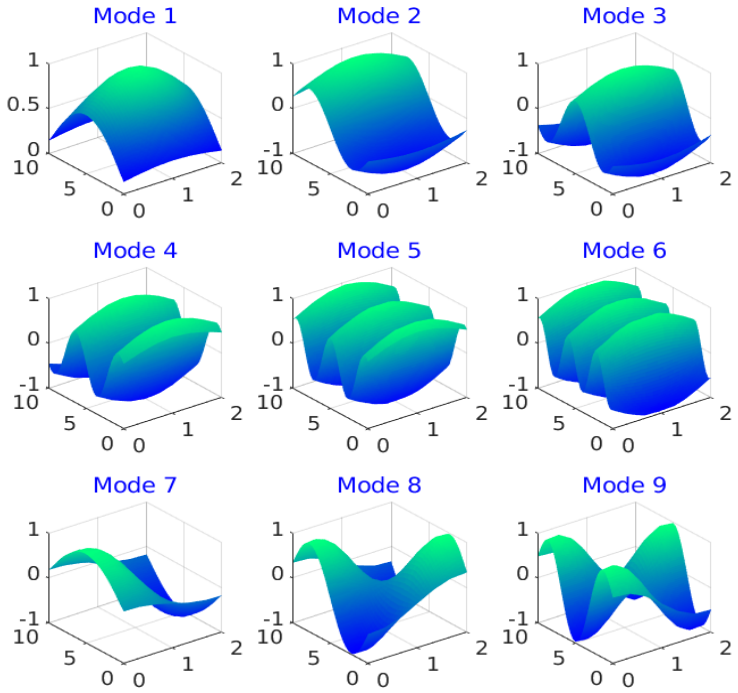


Fig. 6 First nine eigen functions

The algorithm in Alg. 1 shows step by step to truncate a random field via the KLE method. It is applied to truncate the Young modulus $E^m(x,y,\omega)$. The mean value of this random field is selected by a value of $\mu E^m = 1\times 10^4$. To guaranteed the positive value of this modulus, the transformation is set up as follows

$$E^m(x,y,\omega) = {}^{\Theta_E(\boldsymbol{x},\omega)}; \quad \Theta_E(\boldsymbol{x},\omega) = \mu_{\Theta_E}(\boldsymbol{x}) + \sum_{i=1}^{\infty}\sigma_i\psi_i(\boldsymbol{x})\theta_{E\,i}(\omega) \tag{23}$$

The full series of Young modulus $E^m(x,y,\omega)$ is truncated via the KLE method. With the given micro-scale mesh Fig. 4(b), there exists a Delaunay triangular mesh, in which all nodes in the Lattice mode mesh stand on. This hidden mesh with corresponding bilinear shape function is key component to compute the Gramian matrix at each hidden triangular element and then assemble over the entire domain to gain the full Gramian matrix G as in step 2. In step 3, the Matérn function is used to compute the correlation between a couple of two given points with respect to correlation length $l_c$. Specifically, to compute the Matérn covariance, the values of non-negative parameter $\mu_c$ and correlation length $l_c$ are selected, respectively, as 1 and 0.4×min($l$,$h$) in which ($l$,$h$) are length and height of geometry. Following steps 4 and 5, all computed eigenvalues are shown in Fig. 7(a), and the corresponding relative cumulative sum of eigenvalues in Fig. 7(b). The first $L$=35 eigenvalues contribute to more than 90% ($\rho_l$=0.9) of the total sum of all eigenvalues. These eigenvalues are selected for coming steps in the algorithm of the Karhunen-Loève Expansion. The truncated form of exponential parameters in random fields are now written as

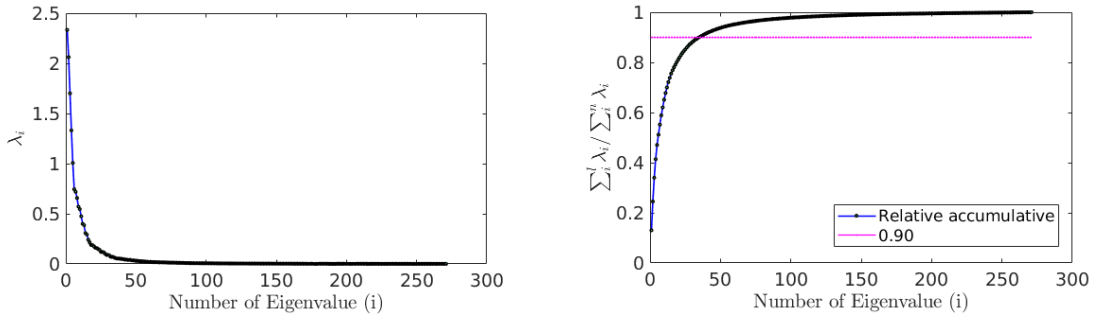


(a) Eigenvalues (b) Relative cumulative sum

Fig. 7 Eigenvalues and desired relative contribution $\rho_L$=0.9

$$\Theta_E(\boldsymbol{x},\omega) = \mu_{\Theta_E}(\boldsymbol{x}) + \sum_{i=1}^{L} \sigma_i \psi_i(\boldsymbol{x}) \theta_{E,i}(\omega) / \rho_L \tag{24}$$

The relative cumulative ration $\rho L$ is added in Eq. (24) to counter the removed 10% contribution. The first nine eigenfunctions are shown in Fig. 6. Each eigenfunction covers a full domain of the given geometry. In the first three responses, they look similar to low-order bi-harmonic functions.

1: Step 1: Import Lattice model mesh with all nodes and set up bilinear shape function $\Psi_i(\boldsymbol{x})$
2: Step 2: Assemble Gramian matrix $\boldsymbol{G}$ over the entire virtual triangular mesh of given Lattice model
3: Step 3: Compute Covariance matrix $\boldsymbol{C}$ via Matérn function
4: Step 4: Solve generalized eigen value problem $\boldsymbol{GCG}\boldsymbol{v}_i = \lambda_i \boldsymbol{G}\boldsymbol{v}_i$
5: Step 5: Truncate expansion with a given limit $\rho_L$
6: Step 6: Generate $L$ basis random Gaussian function $\theta_i$ and complete truncated random field

Alg. 1 Truncating a random field via KLE method

With the selected number $L$=35 of eigenvalues, the corresponding basis random variables $\theta$ are generated. Only $N_\theta^m = 100$ realizations are initiated for each basis random variables of Young modulus using Gaussian distribution $N(0, \sigma_{\theta_E})$. From the computed eigen functions, the random fields including bulk and shear moduli are generated after truncation, see Eq. (7). One realization of the Young modulus $E^m(x, y, \omega)$ is in Fig. 9. It is noted that the realization of Young modulus is computed with the low variance $\mathrm{var}(\Theta)$. The realizations of truncated Young modulus are inserted to corresponding $N^m$ input files for simulation. The geometry, mesh, and boundary conditions remain the same throughout all input files.

### *3.2 Upscaling in the elastic regime*

The updating processes are divided into two main phases. The first phase is to identify bulk and shear moduli $(K^M(\omega), G^M(\omega))$ in the elastic regime, while the second one is to assimilate yield

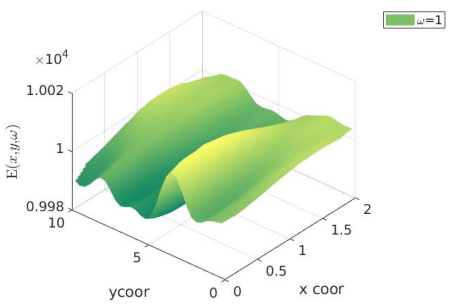


Fig. 8 One realization of random field Young modulus $E^m(x, y, \omega)$

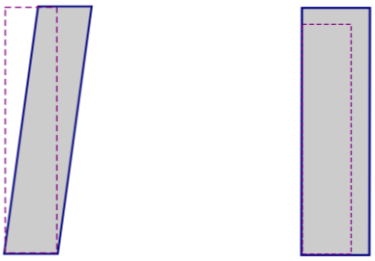

(a) Experiment 1: Shear test (b) Experiment 2: Expansion test

Fig. 9 Experiment setup in elastic regime to identify ($K^M$,$G^M$)

stress $\sigma_y(\omega)$, linear hardening modulus $\mathrm{H}_h(\omega)$, kinematic hardening modulus $\mathrm{H}_k(\omega)$, and visco-plasticity parameter $\eta(\omega)$ and under the inelastic regime. In the macro-scale $\Omega^M$, both bulk and shear moduli are considered as random variables $(K^M(\omega), G^M(\omega))$, which means that they are constant over the entire domain in each simulation. Firstly, the surrogate model of QoI (stored energy) is prepared as a function of simultaneously both bulk and shear moduli $(K^M(\omega), G^M(\omega))$. To ensure the positive value of both moduli, they are configured as exponential functions of input parameters $(q_K(\omega), q_G(\omega))$, which the latter can be modeled as the Gaussian distribution. With this approach, the distributions of $(K^M(\omega), G^M(\omega))$, in fact, are of Lognormal distribution. The mapping is written as follows

$$\begin{aligned} K^M(\omega) &= e^{\Theta_K(\omega)} \qquad \Theta_K(\omega) = \mu_{\Theta_K} + \sigma_{\Theta_K} q(\omega) \\ G^M(\omega) &= e^{\Theta_G(\omega)} \qquad \Theta_G(\omega) = \mu_{\Theta_G} + \sigma_{\Theta_G} q(\omega) \end{aligned} \tag{25}$$

Firstly, the surrogate model of QoI, which is the stored energy $\hat{E}$ at each time step, is formed via the PCE approach as shown in Alg. 2. The data of QoI is stored in the form of $y = [\hat{E}_1\ \hat{E}_2\ \ \hat{E}_n]$, with $n$ as the number of time steps in each simulation.

1: Step 1: Define prior distribution of $(q_K, q_G)$ as Gaussian distributions, e.g. $K = e^{qK}$ and $G = e^{qG}$
2: Step 2: Specify orthogonal basis polynomials, e.g. multi-variable Hermite functions $\boldsymbol{\Phi}_\alpha^q(\boldsymbol{\xi})$
3: Step 3: Compute squared norms and generate integration points with weights $(\boldsymbol{\xi}, \boldsymbol{w})$
4: Step 4: Compute measurable response QoI by FEM solver at integration points
5: Step 5: Obtain PCE coefficients $\boldsymbol{\Upsilon}$ of QoI $\boldsymbol{y}$

Alg. 2 Generating surrogate model of QoI via PCE

After getting the PCE model of QoI, the Gauss-Markov-Kalman filter can be proceeded with step by step shown in Alg. 3.

1: Step 1: Define error model $\boldsymbol{\epsilon}(\boldsymbol{\eta})$ in PCE form
2: Step 2: Fuse different germs into a unified form $\hat{\Phi}(\boldsymbol{\xi}, \boldsymbol{\eta})$
3: Step 3: Update forms of random variables $\hat{\boldsymbol{E}}$, $\hat{\boldsymbol{Q}}$ and $\hat{\boldsymbol{Y}}$ compatible with corresponding new germs $\hat{\Phi}(\boldsymbol{\xi}, \boldsymbol{\eta})$
4: Step 4: Compute Kalman gain $\boldsymbol{K}$
5: Step 5: Update or assimilate PCE coefficients $\hat{\boldsymbol{Q}}'$ of input parameter $(\hat{q}_K, \hat{q}_G)$ after filtering via $\boldsymbol{K}$

Alg. 3 Updating PCE coefficients of input parameters $\mathbf{q}(q_K, q_G)$

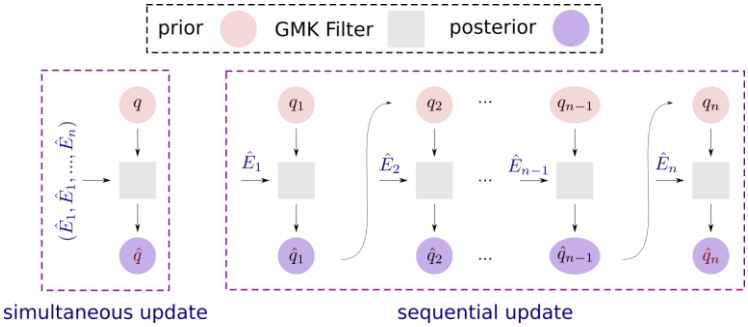


Fig. 10 Simultaneous and sequential update approaches

The numerical experiments are set up to identify the bulk and shear moduli in the macro-scale. Firstly, the shear test is proceeded to identify both moduli. This test would yield a good assimilation value of shear modulus, since it brings a lot of information about the shear modulus. Afterward, both bulk and shear moduli are considered as random variables in the second experiment where the posterior values of both bulk and shear moduli from previous test are input as prior values for the current expansion test. In the shear test, the load is applied via the imposed displacement within 20 time steps at the top of the domain. Then, the expansion test is conducted via applying imposed displacement perpendicular to both right and top edges. The max imposed displacement in both cases is $u$=0.1.

Basically, there are two updating approaches. The first type is to use simultaneously all stored energies and update only once, this method can be called the simultaneous update. Meanwhile, the second type is named as the sequential update. In detail, only stored energy at the first time step from the micro-scale model is inserted into the Gauss-Markov-Kalman filter as QoI. In the next update, the newly assimilated or the posterior PCE coefficients of the input parameter $\hat{Q}'$ are introduced as the prior values to the next update with corresponding stored energy at the second time step. This procedure is repeated until all stored energies are used. Both approaches are illustrated in Fig. 10. In the following, the second approach is employed.

### *3.2.1 Upscaling one realization of $E^m(\omega)$ on the micro-scale $\Omega^m$*

In the following, only one realization of Young modulus with a value of $1\times10^4$, is introduced to the micro-scale $\Omega^m$ over the entire domain. The stored energy responses from both shear and expansion tests are shown in Fig. 11.

The prior values of bulk and shear moduli in the macro-scale are given in Table 3. After updating, the assimilated of shear modulus get more confident with a low value of variance, see

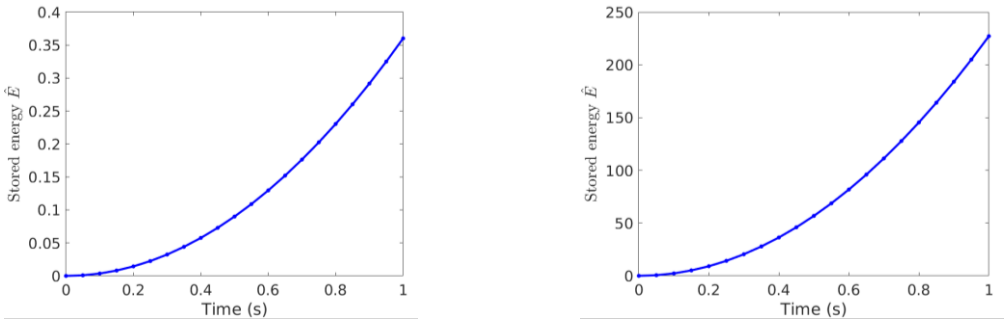


(a) Shear test (b) Expansion test

Fig. 11 One ensemble of $E^m$: Stored energy responses

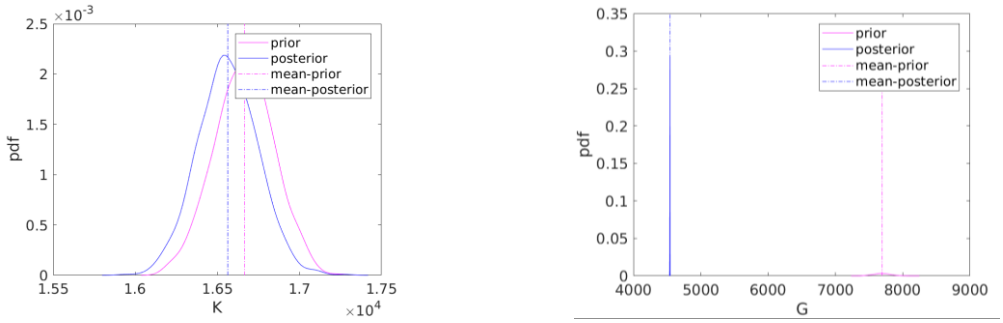


(a) Bulk modulus $K^M$ (b) Shear modulus $G^M$

Fig. 12 Prior and posterior pdf in shear test

Table 3 Bulk and shear moduli ($K^M$,$G^M$) in shear test

| Property | Prior $\mu$ | Prior $\sigma$ | Posterior $\hat{\mu}$ | Posterior $\hat{\sigma}$ |
|---|---|---|---|---|
| Bulk modulus $K^M$ | $1.66 \times 10^4$ | 182 | $1.65 \times 10^4$ | 180 |
| Shear modulus $G^M$ | $7.69 \times 10^3$ | 124 | $4.54 \times 10^3$ | 1.34 |

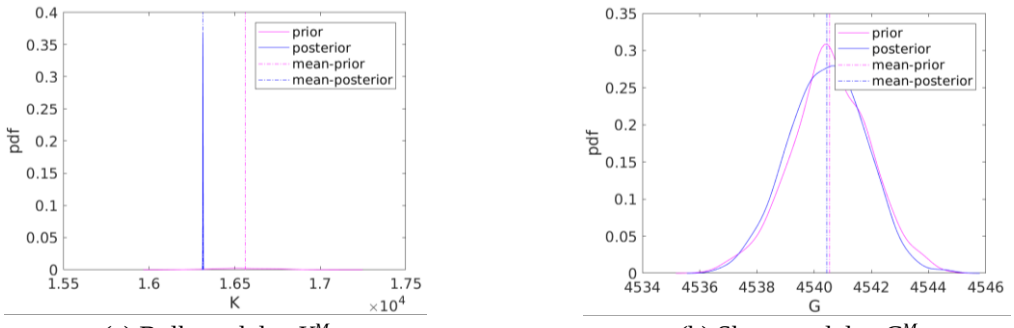


(a) Bulk modulus $K^M$ (b) Shear modulus $G^M$

Fig. 13 Prior and posterior pdf in shear test

Fig. 12(b). However, it is not the case for bulk modulus, see Fig. 12(a). This phenomenon can be explained since the shear test brings less information on the bulk modulus $K^M$.

Table 4 Bulk and shear moduli ($K^M$,$G^M$) in expansion test

| Property | Prior $\mu$ | Prior $\sigma$ | Posterior $\hat{\mu}$ | Posterior $\hat{\sigma}$ |
|---|---|---|---|---|
| Bulk modulus $K^M$ | $1.65 \times 10^4$ | 180 | $1.63 \times 10^4$ | 1 |
| Shear modulus $G^M$ | $4.54 \times 10^3$ | 1.34 | $4.54 \times 10^3$ | 1.33 |

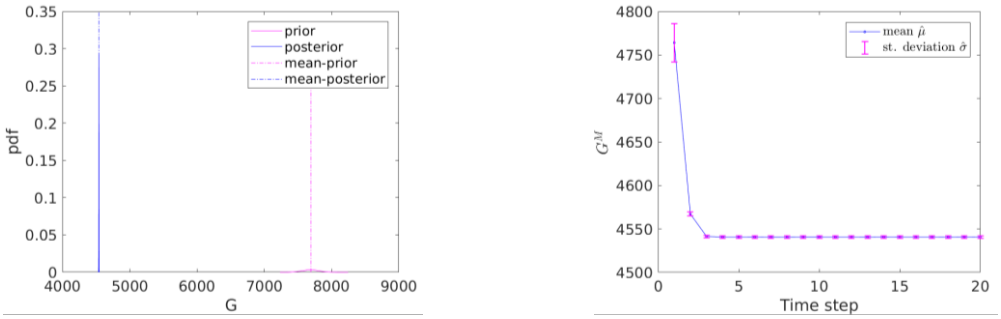


(a) pdf (b) Mean and standard deviation

Fig. 14 Updated shear modulus $G^M$ in shear test

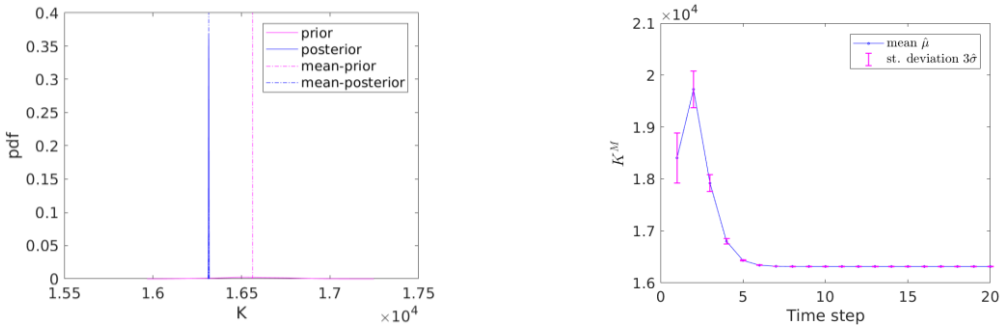


(a) pdf (b) Mean and standard deviation

Fig. 15 Updated bulk modulus $K^M$ in expansion test

Hence, the expansion test is added into further refine the update of both moduli. It is noted that the prior values of both moduli are set by the corresponding posterior values from the shear test. At the end, the variance of bulk modulus $K^M$ shrinks significantly, while the variance of shear modulus $G^M$ still remains relatively small, see Fig. 13.

The posterior values after updating via the Gauss-Markov-Kalman filter are presented in Table 4. The corresponding mean values of Young modulus $E^M$ and Poisson ratio $\nu^M$ are $1.25\times10^4$ and 0.37, respectively.

The convergences of mean values of bulk and shear moduli ($\hat{\mu}K^M, \hat{\mu}G^M$) are shown in Fig. 14 and Fig. 15. In the shear test, the updated mean value of shear modulus $\hat{\mu}G^M$ converges more quickly, see Fig. 14(b), than that of bulk modulus $\hat{\mu}K^M$ in the expansion test, see Fig. 15(b). The standard deviations ($\hat{\mu}K^M, \hat{\mu}G^M$) also shrink significantly within 20 time steps in both cases.

The prior data in Table 3 and posterior data in Table 4 are assembled in Table 5 to present the successful update of both moduli via the Gauss-Markov-Kalman filter method after using both tests.

Table 5 Updated bulk and shear moduli ($K^M$,$G^M$) after both tests

| Property | Prior $\mu$ | Prior $\sigma$ | Posterior $\hat{\mu}$ | Posterior $\hat{\sigma}$ |
|---|---|---|---|---|
| Bulk modulus $K^M$ | 1.66 × 10 4 | 182 | 1.63 × 10 4 | 1 |
| Shear modulus $G^M$ | 7.69 × 10 3 | 124 | 4.54 × 10 3 | 1.33 |

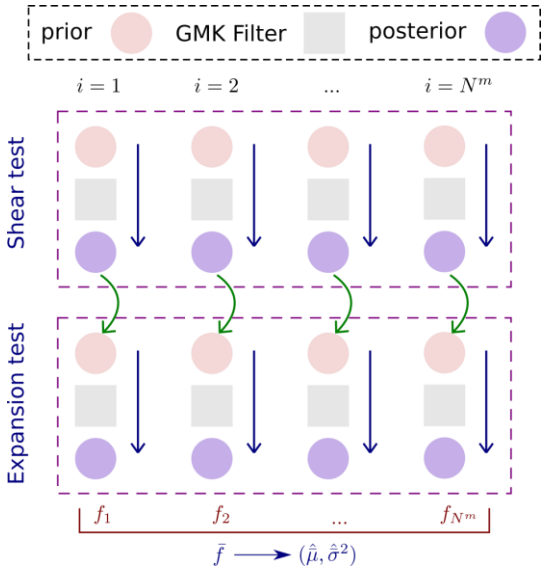


Fig. 16 Flow of data in both tests

### *3.2.2 Upscaling an ensemble of $E^m(x, y, \omega)$ on the micro-scale $\Omega^m$*

In the following the framework of Gauss-Markov-Kalman filter, all relevant random variables in the model are represented via PCE. Hence the filter can be computed with these PCE coefficients in order to update the PCE coefficients of the targeted random variables. This method is applied without any sampling work, contrary to other approaches, e.g., the Ensemble Kalman Filter (EnKF).

To propagate the more uncertainty in the micro-scale $\Omega^m$, the Young modulus $E^m$ is generated as a random field. In micro-scale $\Omega^m$, there are $N^m$ numerical simulations in total. In each simulation, the stored energy $\hat{E}$ is saved into the data-base. At the beginning, the shear test is conducted. The upscaling procedure using the Gauss-Markov-Kalman filter is applied for each set of data from each simulation in mirco-scale. After completing all updates in the shear test, those posterior data are employed as prior data in the expansion test. The same procedure is repeated to update both moduli in the expansion test. The workflow is shown in Fig. 16. After repeating the procedure within $N^m$ times, the final posterior pdf of both bulk and shear moduli are computed via averaging all assimilated pdf as follows

$$\bar{f}_{K^M} = \frac{1}{N^m} \sum_{i=1}^{N^m} f_{i\ K^M} \qquad \bar{f}_{G^M} = \frac{1}{N^m} \sum_{i=1}^{N^m} f_{i\ G^M} \tag{26}$$

From these average pdf, the corresponding mean and variance $(\hat{\bar{\mu}}, \hat{\bar{\sigma}}^2)$ are computed. For the discrete pdf, the formulation of mean and variance are given as

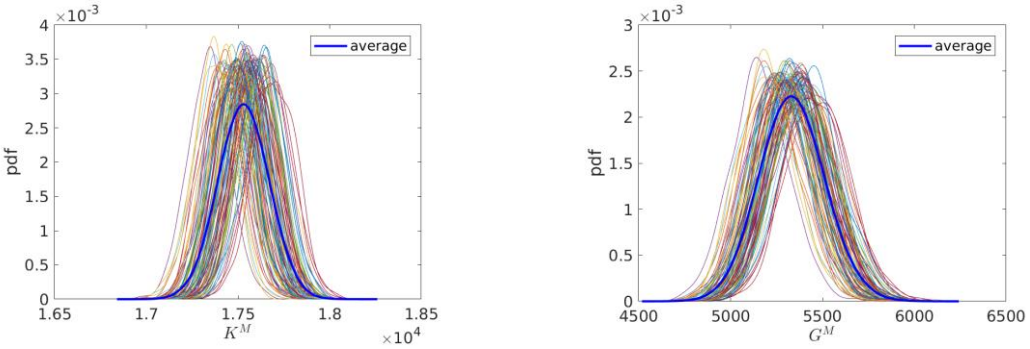


(a) Bulk modulus $K^M$ (b) Shear modulus $G^M$

Fig. 17 Posterior and average pdf after both tests

Table 6 Bulk and shear moduli ($K^M$,$G^M$) after both tests

| Property from average pdf | Mean $\bar{\bar{\mu}}$ | Variance $\bar{\bar{\sigma}}$ |
|---|---|---|
| Bulk modulus $K^M$ | $1.75 \times 10^4$ | 140 |
| Shear modulus $G^M$ | $5.33 \times 10^3$ | 179 |

$$\bar{\bar{\mu}} = \sum_{i=1}^{N^m} \bar{f}_i x_i \qquad \bar{\bar{\sigma}}^2 = \sum_{i=1}^{N^m} \bar{f}_i (x_i - \bar{\bar{\mu}})^2 \tag{27}$$

It is noted that the average pdf $\bar{f}$ is normalized so that $\sum_{i-1}^{N^m} \bar{f}_i = 1$.

Since the shear test gives little information on the bulk modulus $K^M$, the pdf remains nearly the same in all updating steps. Meanwhile the variance of shear modulus $G^M$ shrinks in each update. The posterior from each update in the previous shear test is used as corresponding prior pdf for the expansion test. The average pdf of all updates is given in Table 6 in which both mean and variance are computed from the average pdf. To zoom in the average pdf of both moduli, their values are scaled up 5 times in Fig. 17. Compared to the updates of $(K^M, G^M)$ from using one realization of $E^M$, the new variances are considered bigger but the mean values remain nearly comparable.

### *3.3 Upscaling in the inelastic regime*

To begin with, the inelastic models used in both scales are briefly described. Additionally, random fields on the micro-scale and targeted random variables on the macro-scale are selected. Only important equations are listed in the following section.

#### *3.3.1 Inelastic model in micro-scale $\Omega^m$*

On the micro-scale, the Lattice model is simulated via the Timoshenko beam capable of linear isotropic hardening plasticity and nonlinear kinematic hardening visco-plasticity, see Hadzalic *et al.* (2018), Hadzalic *et al.* (2019), Hadzalic (2020). It is noted that the additive decomposition of the total strain is applied only to axial and shear strains $(\epsilon, \gamma)$, not for the curvature $\mathcal{K}$. The strain energies due to moment, axial and shear forces are given as

$$\begin{aligned}\psi^m(\kappa) &= \frac{1}{2}\kappa I A^e \kappa;\\ \psi^a(\epsilon, \epsilon^{vp}, \xi^a) &= \frac{1}{2}(\epsilon - \epsilon^{vp}) E A^e (\epsilon - \epsilon^{vp}) + \frac{1}{2}\xi^a H_h^a A^e \xi^a;\\ \psi^s(\gamma, \gamma^{vp}, \xi^s) &= \frac{1}{2}(\gamma - \gamma^{vp}) k_c G A^e (\gamma - \gamma^{vp}) + \frac{1}{2}\xi^s H_h^s A^e \xi^s,\end{aligned} \tag{28}$$

in which $(\xi^a, \xi^s)$ are internal hardening variables of axial and shear forces, and $(H_h^a, H_h^s)$ are hardening moduli for axial and shear forces. It is assumed that there are independent plasticity mechanisms activated by axial and shear forces. The independent yield functions $(\phi^a, \phi^s)$ for axial and shear forces $(N, Q)$ are

$$\begin{aligned}\phi^a(N, \chi^a, q^a) &= |N - \chi^a A^e| - (N_y - q^a A^e) \le 0;\\ \phi^s(Q, \chi^s, q^s) &= |Q - \chi^s A^e| - (Q_y - q^s A^e) \le 0,\end{aligned} \tag{29}$$

in which $(X^a, X^s)$ are back-stress variables. The yield axial and shear forces $(N_y, Q_y)$ are computed from the Lattice yield stress $\sigma_y$. For linear hardening, the stress-like isotropic hardening variables $(q^a, q^s)$ are given as

$$q^a = -H_h^a \xi^a; \quad q^s = -H_h^s \xi^s. \tag{30}$$

The Fredrick-Armstrong Armstrong and Frederick (1966) nonlinear kinematic hardening law is employed as

$$\dot{\chi}^a = H_k^a \dot{\epsilon}^{vp} - H_{nk}^a \dot{\xi}^a \chi^a; \quad \dot{\chi}^s = H_k^s \dot{\gamma}^{vp} - H_{nk}^s \dot{\xi}^s \chi^s. \tag{31}$$

The total dissipation can be written in the general form

$$0 < D = \boldsymbol{\sigma} : \dot{\boldsymbol{\epsilon}} - \dot{\psi}. \tag{32}$$

In the following, all linear hardening moduli are assumed to be one unified value of $\mathrm{H}_y$ to reduce the total number of input variables. Similarly, the values of $(\mathrm{H}_{nk}^a, \mathrm{H}_{nk}^s)$ take one unified value $\mathrm{H}_k$. The list of material properties considered as random fields is given in Table 7, e.g., yield stress in tension, yield stress in compression, yield stress in shear, linear hardening modulus, nonlinear kinematic hardening, and viscosity parameter. The procedure to generate the random field (RV) is similar in Section 3.1.

Table 7 Micro-scale material properties as random fields

| Property | Random field |
|---|---|
| Yield stress in tension | $\sigma_{y,t}^m(x, \omega)$ |
| Yield stress in compression | $\sigma_{y,c}^m y(x, \omega)$ |
| Yield stress in shear | $\sigma_{y,s}^m(x, \omega)$ |
| Linear hardening modulus | $H_h^m(x, \omega)$ |
| Nonlinear hardening modulus | $H_k^m(x, \omega)$ |
| Viscosity coefficient | $\eta^m(x, \omega)$ |

Table 8 Micro-scale: One realization values of $(\sigma_{y,t}^m, \sigma_{y,c}^m, \sigma_{y,s}^m, H_h^m, H_k^m, \eta^m)$

| Property | $\sigma_{y,t}^m$ | $\sigma_{y,c}^m$ | $\sigma_{y,s}^m$ | $H_h^m$ | $H_k^m$ | $\eta^m$ |
|---|---|---|---|---|---|---|
| Value | 1 | 1 | 1 | 1000 | 100 | 1000 |

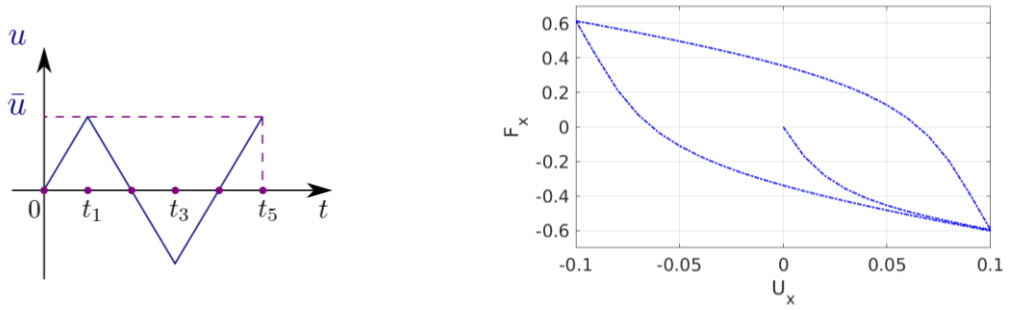


(a) Imposed displacement ū = 0.1 (b) Hysteresis loop

Fig. 18 One realization of $(\sigma_{y,t}^m, \sigma_{y,c}^m, \sigma_{y,s}^m, H_h^m, H_k^m, \eta^m)$: micro-scale responses in inelastic regime by imposed displacement

An example of this Lattice model undergoing a simple shear test $\bar{u} = 0.1$ with one realization of $(\sigma_{y,t}^m, \sigma_{y,c}^m, \sigma_{y,s}^m, H_h^m, H_k^m, \eta^m)$ is shown in Fig. 18. The material properties of $(\sigma_{y,t}^m, \sigma_{y,c}^m, \sigma_{y,s}^m, H_h^m, H_k^m, \eta^m)$ are given in Table 8. It can be seen that the stored energy and dissipation keep increasing in magnitude under loading scenarios. However, they remain nearly the same in unloading scenarios.

### *3.3.2 Inelastic model in macro-scale $\Omega^M$*

In the following, the macro-scale is simulated with the constitutive model of visco-plasticity with capable of linear isotropic hardening and nonlinear kinematic hardening. The enhanced triangular finite element is developed by using the lowest order of Raviart-Thomas vector space to interpolate the stress field, see Nguyen and Ibrahimbegovic (2020). The nonlinear behaviors are formulated in the same manner as the visco-plasticity, see Nguyen and Ibrahimbegovic (2020). By using additive decomposition, the strain energy is written as

$$\psi\left(\mathbf{u}, \boldsymbol{\sigma}, \boldsymbol{\epsilon}^{vp}, \xi^{vp}, \boldsymbol{\zeta}^{vp}\right) = \psi^{e}\left(\boldsymbol{\epsilon}^{e}\right) + \Xi_1^{vp}\left(\xi^{vp}\right) + \Xi_2^{vp}\left(\boldsymbol{\zeta}^{vp}\right), \tag{33}$$

where the relevant internal variables are listed as $\xi^{vp}$ and $\boldsymbol{\zeta}^{vp}$. We also consider additional hardening effects as a general case by including the corresponding potentials $\Xi_1^{vp}$ and $\Xi_2^{vp}$. For those potential energies, we select a quadratic form as follows

$$\begin{aligned} \Xi_1^{vp}\left(\xi^{vp}\right) &= \frac{1}{2}\xi^{vp} K^{vp} \xi^{vp}; & q^{vp} &= -\frac{\partial \Xi^{vp}}{\partial \xi^{vp}}; \\ \Xi_2^{vp}\left(\boldsymbol{\zeta}^{vp}\right) &= \frac{1}{3} H^{vp} \boldsymbol{\zeta}^{vp} : \boldsymbol{\zeta}^{vp}; & \boldsymbol{\alpha}^{vp} &= -\frac{\partial \Xi^{vp}}{\partial \boldsymbol{\zeta}^{vp}}, \end{aligned} \tag{34}$$

in which the terms $K^{vp}$ and $H^{vp}$ are the linear hardening and kinematic hardening moduli. Correspondingly, the terms $q^{vp}$ and $\alpha^{vp}$ are the stress-like variable and back-stress tensor in the visco-plastic model. The yield criterion is now written as

Table 9 Macro-scale material properties as random variables

| Property | Random variables |
|---|---|
| Yield stress | $\sigma_y^M(\omega)$ |
| Linear hardening modulus | $\mathrm{H}_h^M(\omega)$ |
| Nonlinear kinematic hardening modulus | $\mathrm{H}_k^M(\omega)$ |
| Visco-plastic parameter | $\gamma^M(\omega)$ |

$$\phi^{vp}(\boldsymbol{\sigma}, q^{vp}, \boldsymbol{\alpha}^{vp}) := \| \operatorname{dev}(\boldsymbol{\sigma}) + \boldsymbol{\alpha}^{vp} \| - (\sigma_y - q^{vp}) \leq 0. \tag{35}$$

The total dissipation can be written in the following form

$$0 < D = \boldsymbol{\sigma} : \dot{\boldsymbol{\epsilon}}^{vp} + q^{vp}\dot{\xi}^{vp} + \boldsymbol{\alpha}^{vp} : \dot{\boldsymbol{\zeta}}^{vp}. \tag{36}$$

The procedure of the penalty method can be used to derive the evolution equations, where the similar approach is applied in Kachanov damage model, see Nguyen and Ibrahimbegovic (2020), and Ibrahimbegovic (2009). The evolution equations of this visco-plastic model are written as follows

$$\begin{aligned}
\mathbf{0} &= \frac{\partial D_\eta^{vp}(\boldsymbol{\sigma}, \cdot)}{\partial \boldsymbol{\sigma}} = -\dot{\boldsymbol{\epsilon}}^{vp} + \frac{1}{\eta^{vp}} < \phi^{vp} > \frac{\partial \phi}{\partial \boldsymbol{\sigma}} \quad \Rightarrow \dot{\boldsymbol{\epsilon}}^{vp} = \frac{1}{\eta^{vp}} < \phi^{vp} > \hat{\boldsymbol{n}} = \boldsymbol{f}_{\boldsymbol{\epsilon}}; \\
\mathbf{0} &= \frac{\partial D_\eta^{vp}(\boldsymbol{\sigma}, \cdot)}{\partial \boldsymbol{\alpha}^{vp}} = -\dot{\boldsymbol{\zeta}}^{vp} + \frac{1}{\eta^{vp}} < \phi^{vp} > \frac{\partial \phi}{\partial \boldsymbol{\alpha}^{vp}} \quad \Rightarrow \dot{\boldsymbol{\zeta}}^{vp} = \frac{1}{\eta^{vp}} < \phi^{vp} > \hat{\boldsymbol{n}} = \boldsymbol{f}_{\boldsymbol{\zeta}}; \\
0 &= \frac{\partial D_\eta^{vp}(\boldsymbol{\sigma}, \cdot)}{\partial q^{vp}} = -\dot{\xi}^{vp} + \frac{1}{\eta^{vp}} < \phi^{vp} > \frac{\partial \phi}{\partial q^{vp}} \quad \Rightarrow \dot{\xi}^{vp} = \frac{1}{\eta^{vp}} < \phi^{vp} >= f_{\xi},
\end{aligned} \tag{37}$$

in which the notation $\hat{n}$ is the unit normal tensor $\hat{n} = \frac{\operatorname{dev}(\sigma)+\alpha^{vp}}{\|\operatorname{dev}(\sigma)+\alpha^{vp}\|}$. The numerical implementation of this model is straightforward. The list of material properties considered as random fields is given in Table 9, e.g., yield stress, linear hardening modulus, nonlinear kinematic hardening modulus, and visco-plastic parameter. These material properties are chosen to be updated via the Gauss-Markov-Kalman filter method. The workflow in the elastic regime is adapted here.

### *3.3.3 Upscaling one realization of* $(\sigma_{y,t}^m, \sigma_{y,c}^m, \sigma_{y,s}^m, H_h^m, H_k^m, \eta^m)$ *on the micro-scale* $\Omega^M$

The boundary condition and loads are illustrated in Fig. 19(a). The bottom edge is fixed, while an imposed displacement $\bar{u}$ is applied on the top edge. The first cycle for an imposed displacement $\mathrm{u}_1$ takes place within $0 \leq t \leq t_4$, see Fig. 19(b). The second and third ones are defined via $t_4 \leq t \leq t_8$ and $t_8 \leq t \leq t_{12}$, respectively. The time step in each cycle is proportional to its loading magnitude so that the rate of loading is maintained, e.g., $\Delta t_3 = 1.4\Delta t_1$ and $\Delta t_2 = 1.2\Delta t_1$. In both cases, the time step in the first cycle is selected with a value of $\Delta t_1 = 0.1$. The load magnitudes are given as $\bar{u}_1 = 0.04$, $\bar{u}_2 = 0.08$ and $\bar{u}_3 = 0.12$, respectively. The response in the micro-scale is shown in Fig. 19(c). The max stored energies and dissipations in three cycles are selected as QoI for the identification process, see Table 10.

At first, only one realization of $(\sigma_{y,t}^m, \sigma_{y,c}^m, \sigma_{y,s}^m, H_h^m, H_k^m, \eta^m)$ is applied over the entire domain of micro-scale $\Omega^m$. The corresponding values of those material properties are given in Table 8. Meanwhile, the Young modulus and Poisson ratio remain the same as in the elastic regime. The

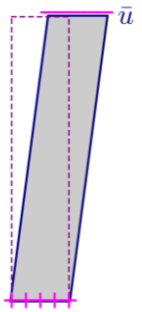


(a) Boundary condition

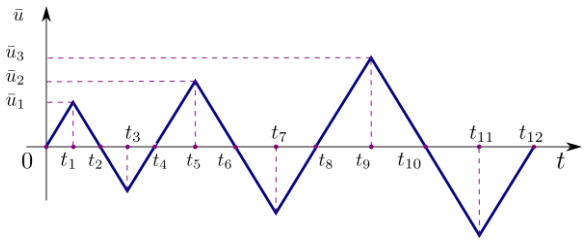


(b) Constant rate of loading

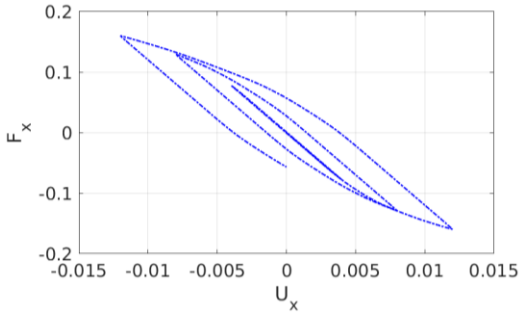


(c) Response in micro-scale

Fig. 19 Experiment setup with imposed displacement $\bar{u}$ in inleastic regime to identify $(\sigma_y^M, H_h^M, H_k^M, \gamma^M)$

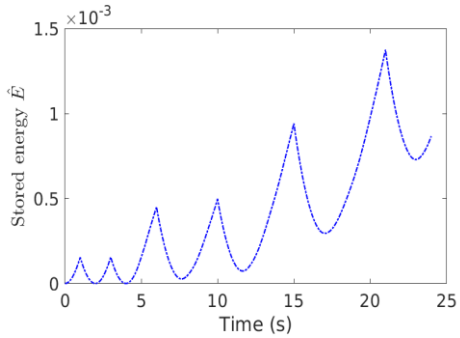


(a) Stored energy

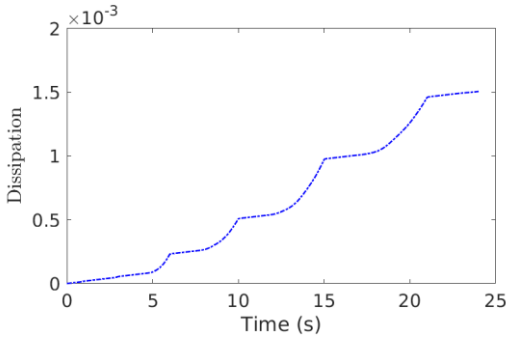


(b) Dissipation

Fig. 20 Micro-scale $\Omega^m$ responses

Table 10 Max stored energy and dissipation in each cycle from micro-scale

| Response | Cycle 1 | Cycle 2 | Cycle 3 |
|---|---|---|---|
| Max $\hat{E}$ | $2\times10^{-4}$ | $5\times10^{-4}$ | $1.4\times10^{-3}$ |
| Dissipation | $1\times10^{-4}$ | $5\times10^{-4}$ | $1.5\times10^{-3}$ |

prior values of all targeted material variables in the macro-scale are given in Table 11. After updating, it is observed that the visco-plastic parameter $\gamma = 1/\eta$ is successfully updated with a smaller variance. The pdf of other parameters remains nearly the same, which means that the

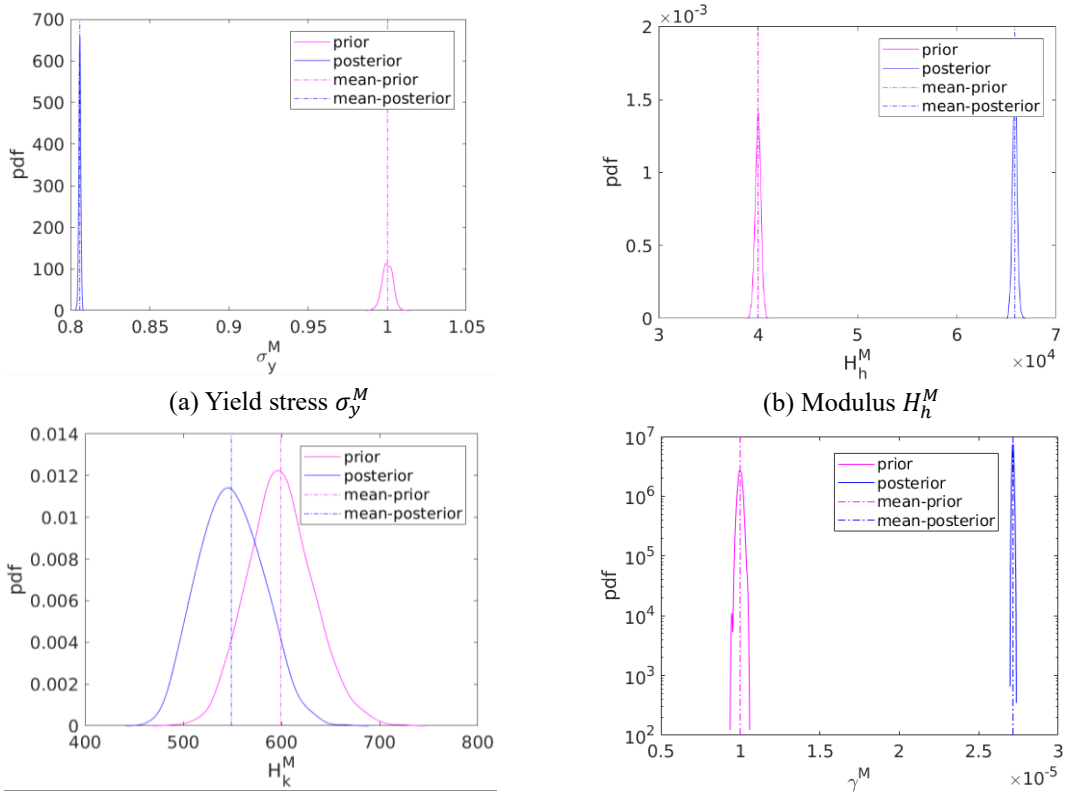


(a) Yield stress $\sigma_y^M$ (b) Modulus $H_h^M$

(c) Modulus $H_k^M$ (d) Vis. para. $\gamma^M$

Fig. 21 Prior and posterior pdf using both stored energy and dissipation as QoI

Table 11 Prior and posterior values of $(\sigma_y^M, H_h^M, H_k^M, \gamma^M)$ using both stored energy and dissipation as QoI

| Property | Prior $\mu$ | Prior $\sigma$ | Posterior $\hat{\mu}$ | Posterior $\hat{\sigma}$ |
|---|---|---|---|---|
| Yield stress $\sigma_y^M$ | 1 | $3.2 \times 10^{-3}$ | 0.8 | $6 \times 10^{-4}$ |
| Modulus $H_h^M$ | $4 \times 10^4$ | 282.8 | $6.6 \times 10^4$ | 227.3 |
| Modulus $H_k^M$ | 600 | 34.6 | 548.9 | 31.9 |
| Visco-plastic parameter $\gamma^M$ | $1 \times 10^{-5}$ | $1.4 \times 10^{-7}$ | $2.7 \times 10^{-5}$ | $5.4 \times 10^{-8}$ |

current experimental test does not contain much information about these parameters.

### *3.3.4 Upscaling an ensemble of $(\sigma_{y,t}^m(x,y,\omega), \sigma_{y,c}^m(x,y,\omega), \sigma_{y,s}^m(x,y,\omega), H_h^m(x,y,\omega), H_k^m(x,y,\omega), \eta^m(x,y,\omega))$ on the micro-scale $\Omega^m$*

On the micro-scale, the parameters $(\sigma_{y,t}^m, \sigma_{y,c}^m, \sigma_{y,s}^m, H_h^m, H_k^m, \eta^m)$ are generated as low-variance random fields in the micro-scale $\Omega^m$. The mean values of these random variables are given in Table 8. The procedure takes place as shown in Fig. 16, where the stored energy and dissipation are used as QoI. The result yields agreement with updated values using one realization of $(\sigma_{y,t}^m, \sigma_{y,c}^m, \sigma_{y,s}^m, H_h^m, H_k^m, \eta^m)$.

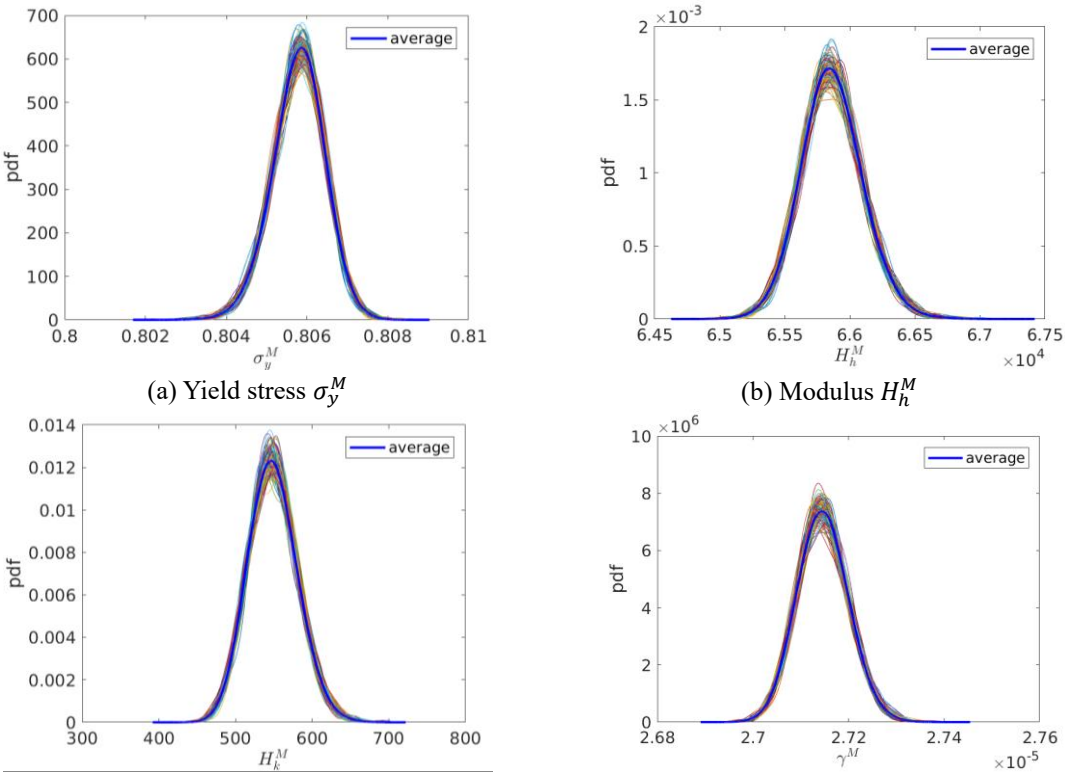


(a) Yield stress $\sigma_y^M$ (b) Modulus $H_h^M$

(c) Modulus $H_k^M$ (d) Visco-plastic parameter $\gamma^M$

Fig. 22 Prior and posterior pdf using an ensemble of random fields

## 4. Conclusions

This work presents a successful feasibility study on the application of parameter identification methods, including the Bayesian update and the Gauss-Markov-Kalman filter, into the upscaling approach for the inelastic and multi-scale problems. In particular, the Bayesian update method is implemented to identify the fracture energy $G_f$ in the simple one-dimensional problem. As an alternative, the Gauss-Markov-Kalman filter is applied in the multi-scale problem. In the micro-scale level, the Lattice model is set up along with the log-normal random fields, such as the Young modulus $E^m(x,y,\omega)$ . In the macro-scale, the mixed triangular membrane element is employed. The finite elements used in both scales are embedded with the visco-plasticity. The material properties in the macro-scale $\Omega^M$ are presented via Gaussian random variables, which are identified by using the stored energy and dissipation as the quantity of interests from the micro-scale $\Omega^m$. In all examples, the proposed approach performs very well.

## Acknowledgments

This work is financially supported under the research project MS3C by Agence Nationale de la Recherche (ANR-20-CE46-0012-01), MEAE (project CESPA), IUF (project MS1479) and the

research fund from the Institute of Scientific Computing, Technical University of Braunschweig. All this support is gratefully acknowledged. These sources of funding are gratefully acknowledged.

## References

Armstrong, P.J. and Frederick, C.O. (1966). *A Mathematical Representation of the Multiaxial Bauschinger Effect*, Vol. 731, Berkeley Nuclear Laboratories, Berkeley, CA.

Bui, D.K., Nguyen, T.N., Ngo, T.D. and Nguyen, X.H. (2020), "An artificial neural network (ANN) expert system enhanced with the electromagnetism-based firefly algorithm (EFA) for predicting the energy consumption in buildings", *Energy*, **190**, 116370. https://doi.org/10.1016/j.energy.2019.116370.

Chatzigeorgiou, G., Javili, A. and Steinmann, P. (2015), "Multiscale modelling for composites with energetic interfaces at the micro-or nanoscale", *Math. Mech. Solid.*, **20**(9), 1130-1145. https://doi.org/10.1177/1081286513516122.

Chiachio-Ruano, J., Chiachio-Ruano, M. and Sankararaman, S. (2021), *Bayesian Inverse Problems: Fundamentals and Engineering Applications*, CRC Press, USA.

Friedman, N., Kumar, P., Zander, E. and Matthies, H.G. (2016), "Bayesian calibration of model coefficients for a simulation of flow over porous material involving SVM classification", *PAMM*, **16**(1), 669-670. https://doi.org/10.1002/pamm.201610323.

Galetzka, A., Bontinck, Z., Römer, U. and Schöps, S. (2019), "A multilevel Monte-Carlo method for high-dimensional uncertainty quantification of low-frequency electromagnetic devices", *IEEE Trans. Magnet.*, **55**(8), 1-12. https://doi.org/10.1109/TMAG.2019.2911053.

Georg, N. and Römer, U. (2020), "Conformally mapped Polynomial chaos expansions for maxwell's source problem with random input data", *Int. J. Numer. Model.: Electr. Network., Dev. Field.*, **33**(6), 2776. https://doi.org/10.1002/jnm.2776.

Gerasimov, T., Römer, U., Vondřejc, J., Matthies, H.G. and De Lorenzis, L. (2020), "Stochastic phase-field modeling of brittle fracture: Computing multiple crack patterns and their probabilities", *Comput. Meth. Appl. Mech. Eng.*, **372**, 113353. https://doi.org/10.1016/j.cma.2020.113353.

Ghanem, R., Soize, C., Mehrez, L. and Aitharaju, V. (2020), "Probabilistic learning and updating of a digital twin for composite material systems", *Int. J. Numer. Meth. Eng*., 1-17. https://doi.org/10.1002/nme.6430.

Goswami, S., Anitescu, C., Chakraborty, S. and Rabczuk, T. (2020), "Transfer learning enhanced physics informed neural network for phase-field modeling of fracture", *Theor. Appl. Fract. Mech.*, **106**, 102447. https://doi.org/10.1016/j.tafmec.2019.102447.

Gravemeier, V., Gee, M.W., Kronbichler, M. and Wall, W.A. (2010), "An algebraic variational multiscale-multigrid method for large eddy simulation of turbulent flow", *Comput. Meth. Appl. Mech. Eng.*, **199**(13-16), 853-864. https://doi.org/10.1016/j.cma.2009.05.017.

Hadzalic, E., Ibrahimbegovic, A. and Dolarevic, S. (2018), "Fluid-structure interaction system predicting both internal pore pressure and outside hydrodynamic pressure", *Couple. Syst. Mech.*, **7**, 659-668. https://doi.org/10.12989/csm.2018.7.6.649.

Hadzalic, E., Ibrahimbegovic, A. and Dolarevic, S. (2019), "Theoretical formulation and seamless discrete approximation for localized failure of saturated poro-plastic structure interacting with reservoir", *Comput. Struct.*, **214**, 73-93. https://doi.org/10.1016/j.compstruc.2019.01.003.

Hadzalic, E., Ibrahimbegovic, A. and Dolarevic, S. (2020), "3D thermo-hydro-mechanical coupled discrete beam lattice model of saturated poro-plastic medium", *Couple. Syst. Mech.*, **9**, 113-134. https://doi.org/10.12989/csm.2020.9.2.125.

Hoang, T.V. and Matthies, H.G. (2021), "An efficient computational method for parameter identification in the context of random set theory via Bayesian inversion", *Int. J. Uncertain. Quantif.*, **11**(4), 1-18. https://doi.org/10.1615/Int.J.UncertaintyQuantification.2020031869.

Hoang, T.V., Krumscheid, S., Matthies, H.G. and Tempone, R. (2021), "Machine learning-based conditional

mean filter: A generalization of the ensemble kalman filter for nonlinear data assimilation", *Proc. Appl. Math. Mech.*, **20**, 1. https://doi.org/10.1002/pamm.202000320.

Ibrahimbegovic, A. (2009), *Nonlinear Solid Mechanics: Theoretical Formulations and Finite Element Solution Methods*, Springer Science & Business Media, Dordrecht, Netherland.

Ibrahimbegovic, A. and Matthies, H.G. (2017), "Probabilistic multiscale analysis of inelastic localized failure in solid mechanics", *Comput. Assist. Meth. Eng. Sci.*, **19**(3), 277-304.

Ibrahimbegovic, A., Matthies, H.G. and Karavelić, E. (2020), "Reduced model of macro-scale stochastic plasticity identification by Bayesian inference: Application to quasi-brittle failure of concrete", *Comput. Meth. Appl. Mech. Eng.*, **372**, 113428. https://doi.org/10.1016/j.cma.2020.113428.

Ibrahimbegovic, A., Niekamp, R., Kassiotis, C., Markovic, D. and Matthies, H.G. (2014), "Code-coupling strategy for efficient development of computer software in multiscale and multiphysics nonlinear evolution problems in computational mechanics", *Adv. Eng. Softw.*, **72**, 8-17. https://doi.org/10.1016/j.advengsoft.2013.06.014.

Ibrahimbegovic, A., Rukavina, I. and Suljevic. S. (2021), "Multiscale model with embedded discontinuity discrete approximation capable of representing full set of 3d failure modes for heterogeneous materials with no scale separation", *Int. J. Multisc. Comput. Eng*., 1-32. https://doi.org/10.1615/IntJMultCompEng.2021038378.

Jänicke, R., Diebels, S., Sehlhorst, H.G. and Düster, A. (2009), "Two-scale modelling of micromorphic continua", *Continuum Mech. Thermodyn.*, **21**(4), 297-315. https://doi.org/10.1007/s00161-009-0114-4.

Jänicke, R., Larsson, F. and Runesson, K. (2020), "A poro-viscoelastic substitute model of fine-scale poroelasticity obtained from homogenization and numerical model reduction", *Comput. Mech.*, **65**(4), 1063-1083. https://doi.org/10.1007/s00466-019-01808-x.

Janouchová, E., Sỳkora, J. and Kučerová, A. (2018), "Polynomial chaos in evaluating failure probability: A comparative study", *Appl. Math.*, **63**(6), 713-737. https://doi.org/10.21136/AM.2018.0335-17.

Kim, J. and Song, J. (2021), "Quantile surrogates and sensitivity by adaptive gaussian process for efficient reliability-based design optimization", *Mech. Syst. Signal Pr.*, **161**, 107962. https://doi.org/10.1016/j.ymssp.2021.107962.

Klinge, S., Bartels, A. and Steinmann, P. (2012), "Modeling of curing processes based on a multi-field potential. single-and multiscale aspects", *Int. J. Solid. Struct.*, **49**(17), 2320-2333. https://doi.org/10.1016/j.ijsolstr.2012.04.034.

Kowalsky, U., Zümendorf, T. and Dinkler, D. (2007), "Random fluctuations of material behaviour in fe-damage-analysis", *Comput. Mater. Sci.*, **39**(1), 8-16. https://doi.org/10.1016/j.commatsci.2006.05.004.

Kožar, I., Bede, N., Bogdanić, A. and Mrakovčić, S. (2021), "Data driven inverse stochastic models for fiber reinforced concrete", *Couple. Syst. Mech.*, **10**(6), 509-520. https://doi.org/10.12989/csm.2021.10.6.509.

Kučerová, A. and Lepš, M. (2014), "Soft computing-based calibration of microplane m4 model parameters: Methodology and validation", *Adv. Eng. Softw.*, **72**, 226-235. https://doi.org/10.1016/j.advengsoft.2014.01.013.

Kumar, P., Friedman, N., Zander, E. and Radespiel, R. (2018), "Bayesian calibration of volume averaged RANS model parameters for turbulent flow simulations over porous materials", *New Results in Numerical and Experimental Fluid Mechanics XI*, 479-488.

Le, T.T. and Le, M.V. (2021), "Development of user-friendly kernel-based gaussian process regression model for prediction of load-bearing capacity of square concrete-filled steel tubular members", *Mater. Struct.*, **54**(2), 1-24. https://doi.org/10.1617/s11527-021-01646-5.

Mareš, T., Janouchová, E. and Kučerová, A. (2016), "Artificial neural networks in the calibration of nonlinear mechanical models", *Adv. Eng. Softw.*, **95**, 68-81. https://doi.org/10.1016/j.advengsoft.2016.01.017.

Marsili, F., Friedman, N. and Croce, P. (2015), "Parameter identification via gPCE-based stochastic inverse methods for reliability assessment of existing structures", *International Probabilistic Workshop*, 112-123. https://doi.org/10.13140/RG.2.1.1843.5600.

Matthies, H.G., Litvinenko, A., Rosic, B.V. and Zander, E. (2016), "Bayesian parameter estimation via filtering and functional approximations", *arXiv preprint*, arXiv:1611.09293.

https://doi.org/10.48550/arXiv.1611.09293.
Matthies, H.G., Zander, E., Rosic, B.V. and Litvinenko, A. (2016), "Parameter estimation via conditional expectation: a Bayesian inversion", *Adv. Model. Simul. Eng. Sci.*, **3**(1), 1-21. https://doi.org/10.1186/s40323-016-0075-7.
Matthies, H.G., Zander, E., Rosic, B.V., Litvinenko, A. and Pajonk, O. (2016), "Inverse problems in a Bayesian setting", *Comput. Meth. Solid. Fluid.*, 245-286. https://doi.org/10.1007/978-3-319-27996-1_10.
Nguyen, C.U. and Ibrahimbegovic, A. (2020), "Hybrid-stress triangular finite element with enhanced performance for statics and dynamics", *Comput. Meth. Appl. Mech. Eng.*, **372**, 11338. https://doi.org/10.1016/j.cma.2020.113381.
Nguyen, C.U. and Ibrahimbegovic, A. (2020), "Isotropic damage model of Kachanov: Theoretical formulation and numerical simulation", *The 2020 International Conference on Advances in Coupled Systems Mechanics (ACSM20)*, Seoul, Korea.
Nguyen, C.U. and Ibrahimbegovic, A. (2020), "Visco-plasticity stress-based solid dynamics formulation and time-stepping algorithms for stiff case", *Int. J. Solid. Struct.*, **196-197**, 154-170. https://doi.org/10.1016/j.ijsolstr.2020.04.018.
Nguyen, C.U., Huynh, T.C. and Kim, J.T. (2017), "Damage identification of wind turbine tower using modal properties-based artificial neural networks", *The 13th International Workshop on Advanced Smart Materials and Smart Structures Technology*, Tokyo, Japan.
Nguyen, C.U., Huynh, T.C. and Kim, J.T. (2018), "Vibration-based damage detection in wind turbine towers using artificial neural networks", *Struct. Monit. Mainten.*, **5**(4), 507. https://doi.org/10.12989/smm.2018.5.4.507.
Nguyen, T.V.M., Nguyen, L.T.K., Rabczuk, T. and Zhuang, X. (2020), "A surrogate model for computational homogenization of elastostatics at finite strain using high-dimensional model representation-based neural network", *Int. J. Numer. Meth. Eng.*, **121**(21), 4811-4842. https://doi.org/10.1002/nme.6493.
Noii, N., Khodadadian, A. and Wick, T. (2020), "Bayesian inversion for anisotropic hydraulic phase-field fracture", *Comput. Meth. Appl. Mech. Eng.*, **386**, 114118. https://doi.org/10.1016/j.cma.2021.114118.
Römer, U. (2021), "Methods of uncertainty analysis and quantification", Technical University of Braunschweig, Lecture.
Römer, U., Bollhöfer, M., Sreekumar, H., Blech, C. and Langer, S. (2021), "An adaptive sparse grid rational arnoldi method for uncertainty quantification of dynamical systems in the frequency domain", *Int. J. Numer. Meth. Eng.*, **122**, 5487-5511. https://doi.org/10.1002/nme.6761.
Rosic, B.V., Litvinenko, A., Pajonk, O. and Matthies, H.G. (2012), "Sampling-free linear Bayesian update of polynomial chaos representations", *J. Comput. Phys.*, **231**(17), 5761-5787. https://doi.org/10.1016/j.jcp.2012.04.044.
Rosic, B.V., Sykora, J., Pajonk, O., Kucerova, A. and Matthies, H.G. (2014), "Comparison of numerical approaches to Bayesian updating", Technical University of Braunschweig, Report.
Rukavina, I., Ibrahimbegovic, A., Do, X.N. and Markovic, D. (2019), "Ed-fem multiscale computation procedure for localized failure", *Couple. Syst. Mech.*, **8**(2), 111-127. https://doi.org/10.12989/csm.2019.8.2.111.
Rus, G., Palma, R. and Pérez-Aparicio, J.L. (2006), "Damage identification inverse problem for a piezoelectric material", *Third European Workshop on Structural Health Monitoring*, Granada, Spain.
Sarfaraz, M.S., Rosic, B.V., Matthies, H.G. and Ibrahimbegovic, A. (2018), "Stochastic upscaling via linear Bayesian updating", *Couple. Syst. Mech.*, **7**, 211-231. https://doi.org/10.12989/csm.2018.7.2.211.
Sarfaraz, M.S., Rosic, B.V., Matthies, H.G. and Ibrahimbegovic, A. (2020), "Bayesian stochastic multi-scale analysis via energy considerations", *Adv. Model. Simul. Eng. Sci.*, **7**(1), 1-35. https://doi.org/10.1186/s40323-020-00185-y.
Schott, B., Rasthofer, U., Gravemeier, V. and Wall, W.A. (2015), "A face-oriented stabilized nitsche-type extended variational multiscale method for incompressible two-phase flow", *Int. J. Numer. Meth. Eng.*, **104**(7), 721-748. https://doi.org/10.1002/nme.4789.
Schüler, T., Manke, R., Jänicke, R., Radenberg, M. and Steeb, H. (2013), "Multi-scale modelling of elastic/viscoelastic compounds", *J. Appl. Math. Mech.*, **93**(2-3), 126-137.

https://doi.org/10.1002/zamm.201200055.
Smith, R.C. (2013), *Uncertainty Quantification: Theory, Implementation, and Applications*, SIAM, Philadelphia, USA.
Stabile, G. and Rosic, B.V. (2020), "Bayesian identification of a projection-based reduced order model for computational fluid dynamics", *Comput. Fluid.*, **201**, 104477. https://doi.org/10.1016/j.compfluid.2020.104477.
Wu, T., Rosic, B.V., De Lorenzis, L. and Matthies, H.G. (2021), "Parameter identification for phase-field modeling of fracture: a Bayesian approach with sampling free update", *Comput. Mech.*, **67**(2), 435-453. https://doi.org/10.1007/s00466-020-01942-x.
Xiu, D. (2010), *Numerical Methods for Stochastic Computations*, Princeton University Press, Princeton, New Jersey, USA.
Xiu, D. and Karniadakis, G.E. (2002), "The wiener-askey polynomial chaos for stochastic differential equations", *SIAM J. Scientif. Comput.*, **24**(2), 619-644. https://doi.org/10.1137/S1064827501387826.
Xiu, D. and Karniadakis, G.E. (2002), "The Wiener-Askey polynomial chaos for stochastic differential equations", *SIAM J. Scientif. Comput.*, **14**(2), 619-644. https://doi.org/10.1137/S1064827501387826.
Yi, S.R., Wang, Z. and Song, J. (2019), "Gaussian mixture-based equivalent linearization method (gm-elm) for fragility analysis of structures under nonstationary excitations", *Earthq. Eng. Struct. Dyn.*, **48**(10), 1195-1214. https://doi.org/10.1002/eqe.3185.
Zander, E. (2011), "SGLIB", Institute of Scientific Computing-Technical University of Braunschweig. https://github.com/ezander/sglib-testing.

*CC*